

# Supporting Information for

## **A Porous Dithiine Linked Covalent-Organic Framework as Dynamic Platform for Covalent Polysulfide Anchoring in Lithium Sulfur Battery Cathodes**

Sattwick Haldar<sup>a,\*</sup>, Mingchao Wang<sup>b</sup>, Preeti Bhauriyal<sup>c</sup>, Arpan Hazra<sup>a</sup>, Arafat H. Khan<sup>d</sup>, Volodymyr Bon<sup>a</sup>, Mark A. Isaacs<sup>e,f</sup>, Ankita De<sup>a</sup>, Leonid Shupletsov<sup>a</sup>, Tom Boenke<sup>a,g</sup>, Julia Grothe<sup>a</sup>, Thomas Heine<sup>c</sup>, Eike Brunner<sup>d</sup>, Xinliang Feng<sup>b,h,i</sup>, Renhao Dong<sup>b,j</sup>, Andreas Schneemann<sup>a</sup>, Stefan Kaskel<sup>a,g\*</sup>

<sup>a</sup>Chair of Inorganic Chemistry I, Technische Universität Dresden, 01069 Dresden, Germany

<sup>b</sup>Center for Advancing Electronics Dresden (cfaed) and Faculty of Chemistry and Food Chemistry, Technische Universität Dresden, 01069 Dresden, Germany

<sup>c</sup>Chair of Theoretical Chemistry, Technische Universität Dresden, 01069 Dresden, Germany

<sup>d</sup>Chair of Bioanalytical Chemistry, Technische Universität Dresden, 01069 Dresden, Germany

<sup>e</sup>Department of Chemistry, University College London, London WC1H 0AJ, UK

<sup>f</sup>HarwellXPS, Research Complex at Harwell, Rutherford Appleton Laboratories, Didcot OX11 0FA, UK

<sup>g</sup>Fraunhofer Institute for Material and Beam Technology (IWS), Winterbergstraße 28, 01277, Dresden, Germany

<sup>h</sup>Center for Advancing Electronics Dresden (cfaed) and Faculty of Chemistry and Food Chemistry, Technische Universität Dresden, 01062 Dresden, Germany

<sup>i</sup>Max Planck Institute of Microstructure Physics, 06120 Halle (Saale), Germany

<sup>j</sup>Key Laboratory of Colloid and Interface Chemistry of the Ministry of Education, School of Chemistry and Chemical Engineering, Shandong University, Jinan 250100, China

\*Sattwick Haldar ([sattwick.haldar@tu-dresden.de](mailto:sattwick.haldar@tu-dresden.de))

\*Stefan Kaskel ([stefan.kaskel@tu-dresden.de](mailto:stefan.kaskel@tu-dresden.de))

### Contents:

	Page no
I. Materials, Methods and Instrumentation.	S2-S5
II. Synthesis of the DUT-177 and its model compound.	S5-S7
III. Characterization of DUT-177 and its model compound.	S7-S10
IV. Structure modeling of DUT-177.	S11-S18
V. FESEM and HRTEM Imaging of DUT-177.	S19-S22
VI. Adsorption data analysis.	S23
VII. Electronic energy level calculations and band structure analysis of DUT-177.	S24-S26
VIII. Cyclic Voltammogram of DUT-177 derived coin-cell.	S27
IX. Characterization of model compound before and after sulfurization.	S27-S30
X. Synthesis and characterization of S-DUT-177 or sulfurized DUT-177.	S31-S36
XI. Battery performance of DUT-177 and S-DUT-177 derived coin-cell.	S37-S38

## I. Materials, Methods and Instrumentation.

2,3,5,6-tetrafluoroterephthalonitrile 97 % (TFPN) was purchased from ABCR. Benzene-1,2-dithiol (DHB), N-methyl-2-pyrrolidone (NMP), 1,4-dioxane, 1,3-dioxolane (DOL), dimethoxyethane (DME) (1:1), triethylamine (Et<sub>3</sub>N), ethylene carbonate (EC) and dimethyl carbonate (DMC) were purchased from Sigma-Aldrich. The lithium salts Lithium hexafluorophosphate (LiPF<sub>6</sub>), lithium bis-(trifluoromethanesulfonyl) imide (LiTFSI) and lithium nitrate (LiNO<sub>3</sub>) were purchased from Sigma Aldrich. Super-P-carbon, Polyvinylidene fluoride (PVDF), were purchased from MTI Corporation.

**Solution State Nuclear Magnetic Resonance Spectroscopy.** <sup>1</sup>H Nuclear Magnetic Resonance (NMR) spectra were acquired using a Bruker Avance III HD 300 MHz spectrometer using DMSO-d<sub>6</sub> as the solvent at 25 °C. The chemical shifts were calibrated using the residual proton signal or the <sup>13</sup>C signal of the solvent as an internal reference (DMSO: 2.50 ppm for <sup>1</sup>H-NMR, 39.52 ppm for <sup>13</sup>C-NMR).

### Solid-State <sup>13</sup>C CP-MAS NMR Spectroscopy.

The <sup>13</sup>C-CP-MAS solid-state NMR spectra were acquired using a Bruker Avance 300 MHz spectrometer and a commercial 2.5 mm double-resonance (<sup>1</sup>H-X) MAS (magic angle spinning) probehead at a MAS frequency of 15 kHz. For the <sup>13</sup>C spectrum, 40 K scans are collected at a delay time of 2s (more than five times of <sup>1</sup>H-T<sub>1</sub>) and 4 ms and 50 μs contact time with a ramped cross polarization (CP) pulse sequence at a resonance frequency of 75.47 MHz. All spectra were referenced to (tetramethylsilane) TMS using adamantane as a secondary reference for <sup>13</sup>C, resonating at 29.5 ppm. <sup>13</sup>C spectra are simulated by using the ACD-Labs software.

### Fourier-Transform Infrared Spectroscopy.

FT-IR spectra were measured on a Bruker VERTEX 70 using the ATR technique in the range of 4000–600 cm<sup>-1</sup>. Every spectra was background corrected.

### UV-Vis Spectroscopy.

UV-Vis absorbance spectra were recorded on a Cary 5000 UV-Vis-NIR spectrophotometer equipped with a mercury lamp. Substrates were mixed with BaSO<sub>4</sub> (COF powder to BaSO<sub>4</sub> ratio 1:20). Base line correction was done towards BaSO<sub>4</sub>. Spectra were taken over a wavelength range of 200-850 nm with a 5 min collection time and 1 nm resolution.

### Powder X-ray Diffraction.

Powder X-ray diffraction (PXRD) patterns were recorded on a STOE StadiP in 2θ Bragg-Brentano geometry using Cu Kα1 (λ = 1.54059 Å) radiation at 40 kV and 40 mA. The signals were collected in 2θ range of 1-50 °θ at 0.0131 °θ step scan with exposure time of 97.920 s per step. Samples were pressed into a custom-build sample holder to minimize background.

**Supercritical Drying.** The supercritical drying procedure was performed in a Jumbo Critical Point Dryer 13200JAB (SPI Supplies). Prior to the supercritical drying process, all samples were solvent exchanged to ethanol and placed in POR3 filter crucibles. The drying chamber was first cooled to 17 °C and the filter crucibles containing the samples were placed inside. The chamber was filled with liquid CO<sub>2</sub> and regularly purged over the course of 2 days (3 times per day). The temperature was then raised to 37 °C, resulting in a chamber pressure of around 80 bar. The CO<sub>2</sub> cylinder equipped with a syphon tube was closed, and the pressure was released. The samples were transferred in to an Ar filled glovebox and handled further under inert atmosphere.

### Physisorption experiments.

Nitrogen and carbon dioxide physisorption experiments were carried out using an Autosorb IQ (Quantachrome Instruments) instrument. For each measurement 20-40 mg of COF powder was used. The measurements were carried out at 77 K for N<sub>2</sub> using a liquid nitrogen bath for cooling and at 195 K and 273 K for CO<sub>2</sub> using a slurry from dry ice and isopropanol or a cryostat for cooling, respectively. Materials were previously activated using supercritical CO<sub>2</sub> and the sample cell was filled inside the glovebox. Prior to the measurement samples were activated on a in vacuum at 120 °C for at least 6 hours. Brunauer-Emmett-Teller (BET) surface areas were calculated from the linearized N<sub>2</sub> isotherm at 77 K using AsiQwin software within the pressure range p/p<sub>0</sub> of 0.04–0.12 so that the linear model fit had an R<sup>2</sup> of greater than 0.999. Pore size distribution was calculated from the desorption branch of the N<sub>2</sub> isotherms at 77 K using the BJH method via the AsiQwin software package.

### Single crystal data analysis:

The dataset on the single crystal of the thianthrene molecular model compound was collected at BESSY MX BL14.2 beamline of Helmholtz-Zentrum Berlin für Materialien und Energie at 298 K. A total number of 1800 images using φ-scans with oscillation step

of 0.1° were collected. The dataset was processed in an automatic regime using XDSAPP 3.0 program.<sup>1</sup> The crystal structure was solved by direct methods and refined by full-matrix least-squares on  $F^2$  using SHELX-2018/3 program package.<sup>2</sup> All non-hydrogen atoms were refined in anisotropic approximation. Hydrogen atoms were refined in geometrically calculated positions using the “riding model” with  $U_{iso}(H)=1.2U_{iso}(C)$ . Crystallographic data for the thianthrene molecular model compound (CCDC- 2149889) can be obtained free of charge from the Cambridge Crystallographic Data Centre via [www.ccdc.cam.ac.uk/data\\_request/cif](http://www.ccdc.cam.ac.uk/data_request/cif).

Crystal data for molecular model compound:  $C_{20}H_8N_2S_4$ ,  $M = 404.52 \text{ g mol}^{-1}$ , monoclinic,  $P2_1/c$  (*No14*),  $a = 4.0100(8) \text{ \AA}$ ,  $b = 20.750(4) \text{ \AA}$ ,  $c = 10.080(2) \text{ \AA}$ ,  $\beta = 93.34(3)^\circ$ ,  $V = 837.3(3) \text{ \AA}^3$ ,  $z = 2$ ,  $d = 1.604 \text{ g cm}^{-3}$ ,  $\mu = 0.790 \text{ mm}^{-1}$ ,  $F(000) = 412$ ,  $\vartheta_{max} = 34.667^\circ$ , 6359 / 1936 / 118 reflections collected / unique / parameter,  $R_{int} = 0.0217$ ,  $R1(I > 2\sigma) = 0.0318$ ,  $wR2(all) = 0.3450$ ,  $S = 1.014$ .

### Modeling and electronic structure.

Density functional theory (DFT) calculations are carried out using the Vienna ab-initio Simulation Package (VASP).<sup>3,4</sup> Electron-ion interactions are described using the projector augmented wave (PAW) method<sup>5,6</sup> and the generalized gradient approximation (GGA)<sup>7</sup> of the exchange-correlation energy in the form of Perdew-Burke-Ernzerhoff (PBE)<sup>8</sup> is applied. A convergence threshold of 10<sup>-5</sup> eV in energy and 10<sup>-2</sup> eV  $\text{\AA}^{-1}$  for the force within the conjugated gradient method for geometry optimizations and a cutoff energy of 520 eV for the plane-wave basis set are adopted in all calculations. A Monkhorst-Pack Gamma-centred grid with 1×1×7 dimension is used for k-point sampling of the Brillouin zone for the bulk systems and 1×1×1 dimension for monolayers. Grimme’s D3 van der Waals corrections<sup>9</sup> is used to accurately describe the weak interactions. The DUT-177 monolayers are modelled by adding a large vacuum space of 15  $\text{\AA}$  in the direction normal to the monolayer. The HSE06<sup>10</sup> method is employed to calculate the band structure of the unit cell of 1-layered bulk model with 7 high symmetry points across the Brillouin zone and maintaining 20 kpoints between each two high symmetry points. Molecular calculations are carried out using Gaussian09 D.01<sup>11</sup> and B3LYP/6-31 G\* level of theory. Natural bond orbital (NBO) analysis is done to understand the nature of bonding.<sup>12</sup>

The molecular unit of DUT-177 can have two possible isomers, 1) up-down bending of the thianthrene ring, and 2) all-up-all-down bending of the thianthrene ring, defined as isomer-1 and isomer-2, respectively, as presented in Figure S5. Both of these isomers are energetically favourable with a small energy difference of 0.22 kcal mol<sup>-1</sup> (isomer-1 being 0.22 kcal mol<sup>-1</sup> more energetically stable than isomer-2). We have also calculated the energy barrier for the twisting of thianthrene ring of isomer-1 to form isomer-2 and it amounts to 5.09 kcal mol<sup>-1</sup> as shown in Figure S5C.

For the periodic calculations, two possible monolayers defined as monolayer-1 and monolayer-2 are modelled based on the molecular arrangements of isomer-1 and isomer-2, respectively (Figure S6). The optimized lattice parameters and the relative energy difference are shown in Table S3. Similar to the molecular isomers, the monolayers also have negligible difference (~0.1 kcal/mol per unit cell) in their energetic stability, having the equal possibility of formation. Additionally, the HOMO-LUMO of isomers 1 and 2 and the electronic band structures and projected density of states (PDOS) of corresponding monolayers are plotted in Figure S12 and S13 (A and B), respectively. Both isomers have similar HOMO-LUMO gaps of ~3.54 eV and the monolayers are direct band semiconductors (the valence band (VB) have their extrema at gamma point and PBE band gap ~ 2.0 eV) with a slightly more dispersed VB than the flat conduction band (CB). This implies that in-plane charge transport for monolayers is small. Besides, the bands near to the Fermi level could be easily thermally-populated with holes, indicating a typical p-type semiconducting behaviour.

For the 3D structure of DUT-177, both monolayers, Monolayer-1 and Monolayer-2 are considered and four types of layer-stacking are optimized (AA eclipsed, AA-inclined, AA-serrated and AB-staggered). The unit cell for the 3d structure contains two layers in c direction for AA-serrated, and AB stacking and one layer for AA and AA-inclined stackings. The optimized 3D structures constructed using Monolayer-1 are shown in Figure S8. The relative stability (Table S4) and the corresponding PXRD patterns (Figure S9) for each stacking mode are compared with the experimental one and it is found that the PXRD patterns of AA, AA-inclined and AA-serrated stacked layers fit to the experiment. We focused our discussion on AA-inclined stacking because it is energetically more favourable with a stacking energy of -64.4 kcal mol<sup>-1</sup> over AA and AA-serrated with -61.6 kcal mol<sup>-1</sup> and -61.4 kcal mol<sup>-1</sup>, respectively. Surprisingly, on full cell relaxation, the bulk structures of Monolayer-2 layers (in all four stackings) do not retain the molecular arrangement of parent Monolayer-2, and convert to a local minima structure where in the stacked layers, one of the three thianthrene unit becomes planar as shown in Figure S7. This obtained structure is energetically less favourable by 2.77 kcal mol<sup>-1</sup> than the AA-inclined (of Monolayer-1) structure. From the band structure of the 3D model in AA-inclined stacking mode using HSE06 functional, we find a band gap of 2.45 eV (Fig. 3B in main text).

### SEM and EDX

Scanning electron microscopy (SEM) images were recorded with a SU8020 (Hitachi) operated at an acceleration voltage of 2 kV and a working distance of 8 mm. Energy-dispersive X-ray analysis (EDX) of samples was carried out by AZtec software (Oxford Instruments) with an operating voltage of 15 kV and a working distance of 15 mm. Before SEM and EDX measurements the samples

were dispersed in ethanol and placed on a pre-cleaned Si sample holder and dried overnight at 60 °C. Thereafter, the samples were sputtered with Au to enhance the conductivity.

#### **HR-TEM.**

The HRTEM images were taken with a JEOL Jem F-200C - transmission electron microscope equipped with a Gatan OneView - in-situ 4K camera at an acceleration voltage of 200 kV. The samples were drop-casted on holey carbon Cu-grids from EtOH immediately prior to the imaging.

#### **MALDI-TOF.**

High-resolution MALDI-TOF mass spectrometry was recorded on a Bruker Autoflex Speed MALDI TOF MS (Bruker Daltonics, Bremen, Germany) with trans-2-[3-(4-tert-Butylphenyl)-2-methyl-2-propenylidene] malononitrile as the matrix. The instrument is equipped with an Agilent Series 1200 HPLC binary pump, and Autosampler, using Mass Hunter software.

#### **Raman spectroscopy.**

Raman spectra were recorded using a BRUKER RFS 100 Raman system which consists of a 1064 nm laser for excitation and a liquid nitrogen cooled Ge-detector. Raman spectra were acquired at a wavelength of  $\lambda = 1064$  nm with a resolution of  $4 \text{ cm}^{-1}$  at 400 mW power and 100~200 scans. Due to strong fluorescence of the sample low energy Raman spectroscopy was used (1064 nm).

#### **TG-DTG-MS.**

Thermogravimetric analysis combined with Mass spectra was performed under Nitrogen flow in a temperature range of 298 – 1000 K with a heating rate of 5 K/min using a STA 409 PC (NETZSCH).

#### **XPS analysis.**

The X-ray photoelectron (XPS) data collection was performed at the EPSRC National Facility for XPS (“HarwellIXPS”), operated by Cardiff University and UCL, under Contract No. PR16195. The data was acquired using a Kratos Axis SUPRA using monochromated Al  $\text{K}\alpha$  (1486.69 eV) X-rays at 15 mA emission and 12 kV HT (180W) and a spot size/analysis area of  $700 \times 300 \mu\text{m}$ . The instrument was calibrated to gold metal Au 4f (83.95 eV) and dispersion adjusted to give a BE of 932.6 eV for the Cu 2p<sub>3/2</sub> line of metallic copper. Ag 3d<sub>5/2</sub> line FWHM at 10 eV pass energy was 0.544 eV. Source resolution for monochromatic Al  $\text{K}\alpha$  X-rays is ~0.3 eV. The instrumental resolution was determined to be 0.29 eV at 10 eV pass energy using the Fermi edge of the valence band for metallic silver. Resolution with charge compensation system on <1.33 eV FWHM on PTFE. High resolution spectra were obtained using a pass energy of 20 eV, step size of 0.1 eV and sweep time of 60s, resulting in a line width of 0.696 eV for Au 4f<sub>7/2</sub>, S 2p and S LMM spectra were recorded at a pass energy of 40 eV for the purposes of determining modified auger parameter. Survey spectra were obtained using a pass energy of 160 eV. Charge neutralisation was achieved using an electron flood gun with filament current = 0.38 A, charge balance = 2 V, filament bias = 4.2 V. Successful neutralisation was adjudged by analysing the C 1s region wherein a sharp peak with no lower BE structure was obtained. Spectra have been charge corrected to the main line of the carbon 1s spectrum set to 284.8 eV. All data was recorded at a base pressure of below  $9 \times 10^{-9}$  Torr and a room temperature of 294 K. Data was analysed using CasaXPS v2.3.19PR1.0. Peaks were fit with a Shirley background prior to component analysis. Peaks were fit using a LA(1.53,243) lineshape. S 2p peaks were fit with a doublet separation of 1.15 eV.

#### **Electrochemical measurements:**

The constant current charge-discharge measurements were performed using a LAND BATTERY analyser and data was extracted by LAND BATTERY 7.3 software. The cyclic voltammetry and potentiostatic electrochemical impedance studies were performed on a BioLogic Multichannel electrochemical workstation.

The 2032 coin-cells of derived COFs were utilized for each electrochemical measurements. At first a slurry of composite (75 % DUT-177 or S-DUT-177, 20 % Super-P-carbon, 5 % of Polyvinylidene fluoride (PVDF) in N-Methylpyrrolidone (NMP)) was coated on a carbon coated Aluminum foil using a doctor-blade. After vacuum drying at 45 °C for 3 days the coated portion on the Aluminum foil was cut into circles with a diameter of 12 mm. Then those electrodes were sandwiched together with Lithium foil using 40  $\mu\text{L}$  of electrolyte (1 M lithium hexafluorophosphate ( $\text{LiPF}_6$ ) in ethylene carbonate (EC) : dimethyl carbonate (DMC) (1:1) or 1 M lithium bis-(trifluoromethanesulfonyl)imide ( $\text{LiTFSI}$ ) in dioxolane (DOL) : dimethoxyethane (DME) (1:1) with 0.1 M lithium nitrate ( $\text{LiNO}_3$ )) soaked PTFE (Polytetrafluoroethylene) separator (19 mm sized) and pressed in the aforementioned coin-cell (2032) case. The content of sulfur in the cathode electrodes of S-DUT-177 was calculated to be 0.55 mg/cm<sup>2</sup> which leads to 1.8 mAh/cm<sup>2</sup> sp. capacity @0.25 mA/cm<sup>2</sup> current density. The very fluffy nature of the material could not afford us to increase the

areal loading to enhance the areal capacity. Also, our derived electrode contains a considerable percentage of organic backbone along with the sulfur content. Therefore, the porous material derived electrode soaks the electrolyte easily and causes quick drying of the cell. Hence, electrolyte to sulfur (E/S) was kept higher (16  $\mu\text{L}/\text{mg}_\text{s}$ ) than the practical limit (3  $\mu\text{L}/\text{mg}$ ).

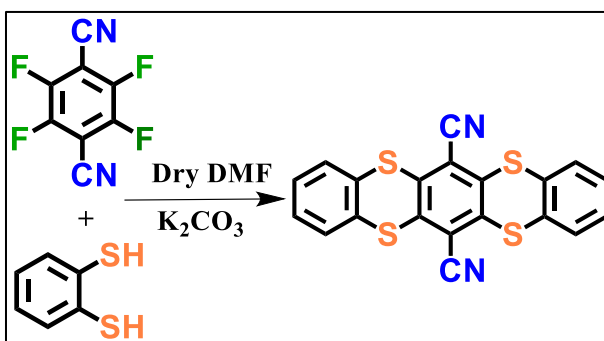
The electrochemical impedance analysis of the prepared coin-cell was performed within the range of 1 MHz to 1000 mHz at the open circuit voltage of the cell. The CV of the coin-cells were operated from 0.025 mV/s to 1 mV/s scan rate in different potential window.

#### Four probe conductivity measurements:

Specific resistivity and conductivity was determined for a DUT-177 pellet (diameter: 1 cm) after compression in a hollow cylinder using a punch press at  $p = 2t$  in a customized set-up. The punch as well as the bottom of the cylinder are the measurement electrodes. The electric resistivity was determined by a Keithley 2400 Source Meter during the compression process between these two electrodes. The measurement range was set to 200 M $\Omega$  at 100 nA. The specific resistivity  $\rho$  (in  $\Omega \cdot \text{cm}$ ) of the material was derived from the measured resistivity  $R$  (in  $\Omega$ ) multiplied with the area  $A$  ( $\text{cm}^2$ ) and divided by the thickness (cm)  $t$  of the pellet. The conductivity  $\sigma$  (S/cm) is the reciprocal of the specific resistivity.

## II. Synthesis of DUT-177 and its model compound.

**Model compound:** The dithiine linked model compound has been synthesized by reacting *ortho*-aryldithiols (Benzene-1,2-dithiol) (1 mmol, 115  $\mu\text{L}$ ) and *ortho*-aryl-tetrafluorides (2,3,5,6-tetrafluoroterephthalonitrile)(0.5 mmol, 100 mg) in dry DMF using potassium carbonate ( $\text{K}_2\text{CO}_3$ ), (3 mmol, 415 mg) as a catalyst. The reaction medium was heated up to 80  $^\circ\text{C}$  for 24 hrs, initiating the substitution of the fluoride ions via the  $\text{S}_\text{N}\text{Ar}$  mechanism which lead to the formation of a bright yellow colored suspension. The compound was precipitated out of the suspension by adding 1M HCl solution and isolated by filtration. The product was then solvent exchanged with dioxane, ethanol, acetone and chloroform to wash out all impurities and unreacted starting materials. Unfortunately the product was not fully soluble in any common organic solvents so characterization by solution state NMR was not feasible. However crystallization from the vapor phase via sublimation (the compound was sealed in an ampoule under  $10^{-4}$  kPa vacuum and heated to 380  $^\circ\text{C}$  for 12 hrs and then slowly cooled to room temperature) produced phase pure rod shaped single crystal of the compound. Therefore the single crystal structure (Figure S1) along with the solid state NMR (Figure S3), IR (Figure S4) and MALDI-TOF (Figure S13) mass spectrometry confirmed the preparation of the non-planar dithiine linkage in the model compound.



Scheme S1. Synthesis of a dithiine linked model compound.

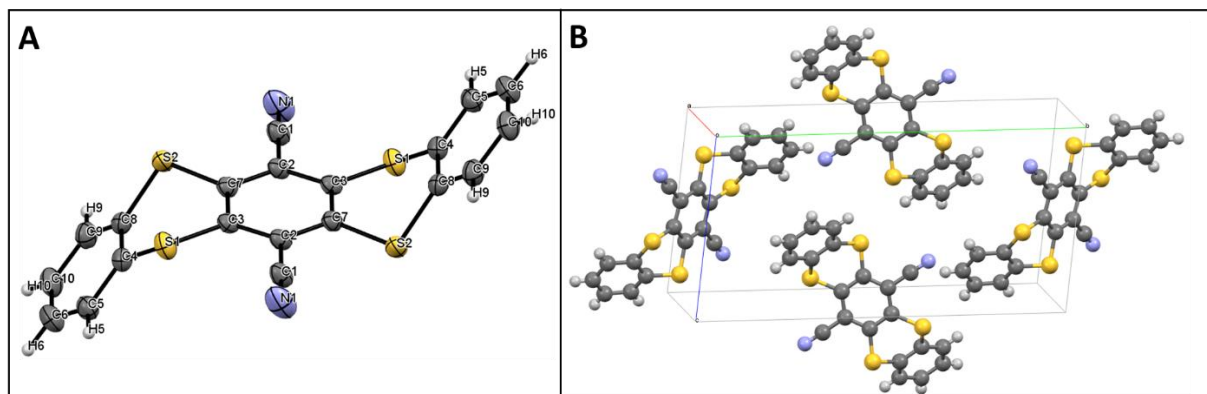


Figure S1: A. Depiction of the single crystal structure of the model compound. Thermal ellipsoids are set at a probability of 50 %. B. Packing of the molecules in the unit cell of the crystal structure of the model compound. C, H, N and S are displayed in grey, white, blue and yellow respectively.

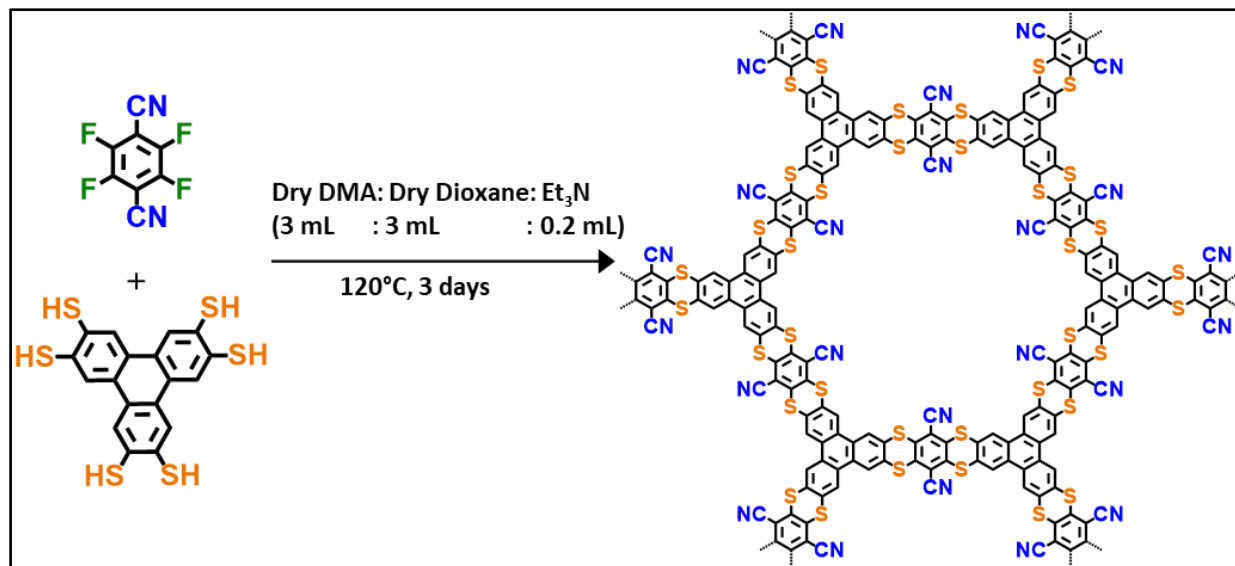
Table S1. Selected bond lengths and angles of the model compound.

Bond length	Å	Valence angle	degree (°)
S1-C3	1.7566(13)	C3-S1-C4	101.41(6)
S1-C4	1.7667(14)	C7-S2-C8	100.90(6)
S2-C7	1.7575(13)	N1-C1-C2	178.22(18)
S2-C8	1.7661(14)	C1-C2-C3	118.89(11)
N1-C1	1.140(2)	C1-C2-C7	119.39(11)
C1-C2	1.4415(18)	C3-C2-C7	121.70(11)
C2-C3	1.4041(17)	S1-C3-C2	119.48(9)
C2-C7	1.4060(18)	S1-C3-C7_a	121.31(9)
C3-C7_a	1.3983(18)	C2-C3-C7_a	119.16(11)
C4-C5	1.3923(18)	S1-C4-C5	118.77(10)
C4-C8_a	1.3935(18)	S1-C4-C8_a	121.22(10)
C5-C6	1.387(2)	C5-C4-C8_a	120.01(12)
C6-C10_a	1.382(2)	C4-C5-C6	119.62(13)
C8-C9	1.394(2)	C5-C6-C10_a	120.22(14)
C9-C10	1.385(2)	S2-C7-C2	119.69(9)

$$a = 1-x, 1-y, 2-z$$

**Thianthrene based COF (DUT-177):** The  $S_NAr$  reaction strategies has been followed to develop a layered 2D-Thianthrene based COF from dithiine linkage. Triphenylene-2,3,6,7,10,11-hexathiol (0.1 mmol, 42.1 mg) and 2,3,5,6-tetrafluoroterephthalonitrile (0.15 mmol, 30 mg) were mixed in DMA (N,N-Dimethylacetamide): 1,4-Dioxane: Et<sub>3</sub>N (3 mL: 3 mL: 0.2 mL) in a 16 cm long

borosilicate ampoule. The mixture was at first frozen by placing the ampoule in a liquid N<sub>2</sub> bath and under dynamic vacuum the ampoule was flame sealed at 10<sup>-3</sup> Torr. The resulting cut ampoule had a length of approximately 12 cm and was sonicated for 15 minutes after thawing of its content. Then the sealed ampoule was placed in a sand bath in an isothermal oven. The temperature inside the oven was raised to 120 °C and maintained for 4 days and afterwards gradually cooled down to room temperature over 12 hrs. During this time a brightly colored orange solid formed inside the ampoule. The solvent inside the sealed ampoule was then again frozen and the ampoule was opened with a glass cutting tool, to obtain the product. The product was then solvent exchanged with dry ethanol for a week followed by supercritical drying. Finally a very fluffy and cotton-like orange product was isolated and stored in an Ar filled glove box. The crystallinity of this COF was confirmed by PXRD (Figure S2). The formation of the dithiine linkage and the presence of all expected functional units were confirmed from solid state NMR (Figure S3) and IR spectroscopy (Figure S4). Elemental Analysis: Theoretical: C: 59.98, H: 1.01, N: 6.99, S: 32.02; Measured C: 53.40, H: 2.21; N: 6.45; S: 24.35. Yield: 55 mg.



**Scheme S2. Synthesis of thianthrene based COF (DUT-177).**

The Triphenylene-2,3,6,7,10,11-hexathiol (THT) linker has been synthesized according to previously reported methods.<sup>13-15</sup>

### III. Characterization of DUT-177 and its model compound.

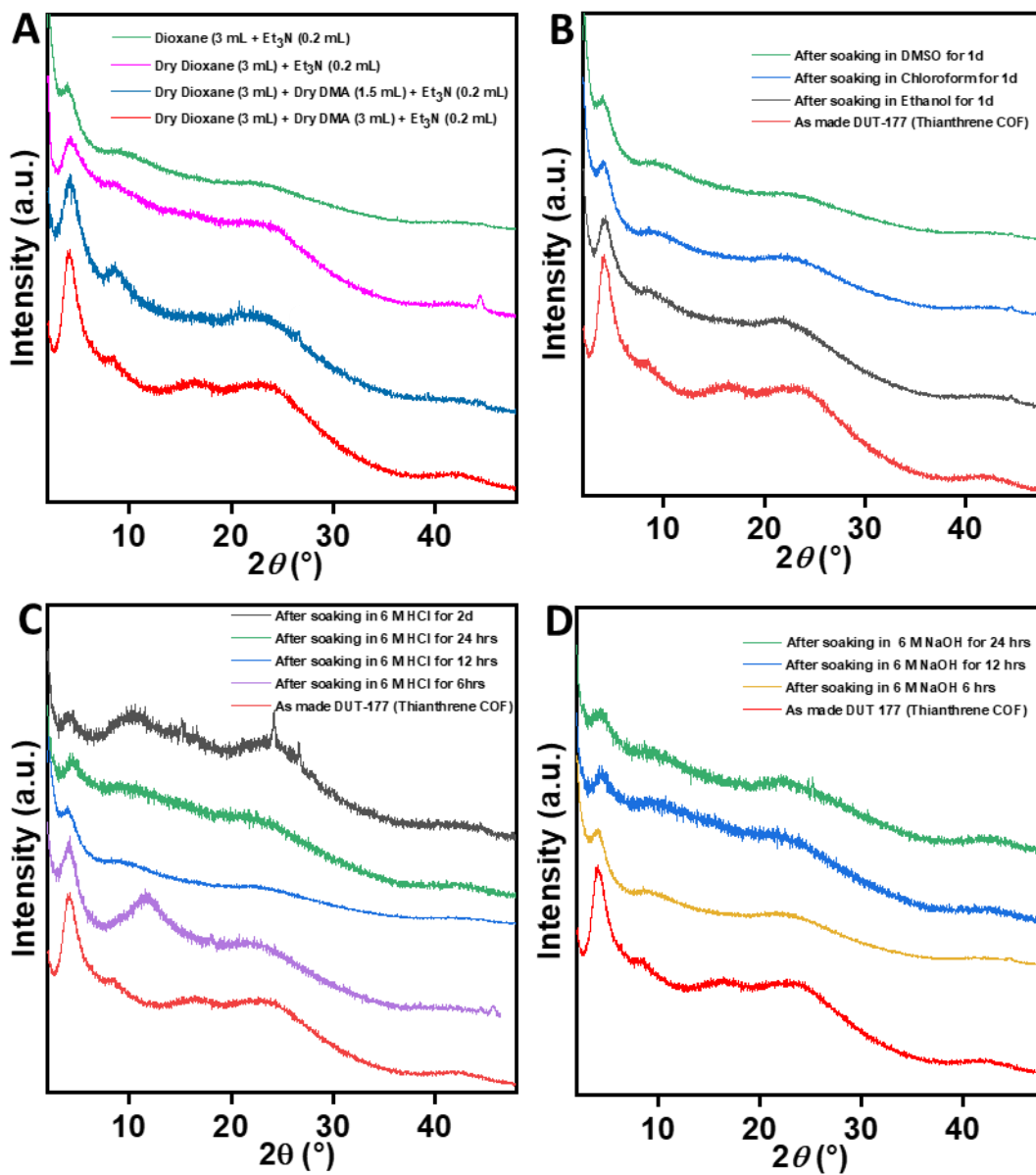


Figure S2. A. Improvement of the crystallinity of DUT-177 by variation of the solvent mixture used during synthesis. The best PXRD for DUT-177 was obtained from Dioxane-DMA (1:1) solvent mixture. B. The crystallinity of DUT-177 after soaking in different organic solvents. C. The crystallinity of DUT-177 after soaking in 6 M hydrochloric acid (HCl) over different amounts of time (HCl). D. Crystallinity of DUT-177 after soaking in 6 M sodium hydroxide (NaOH) over different timespans.

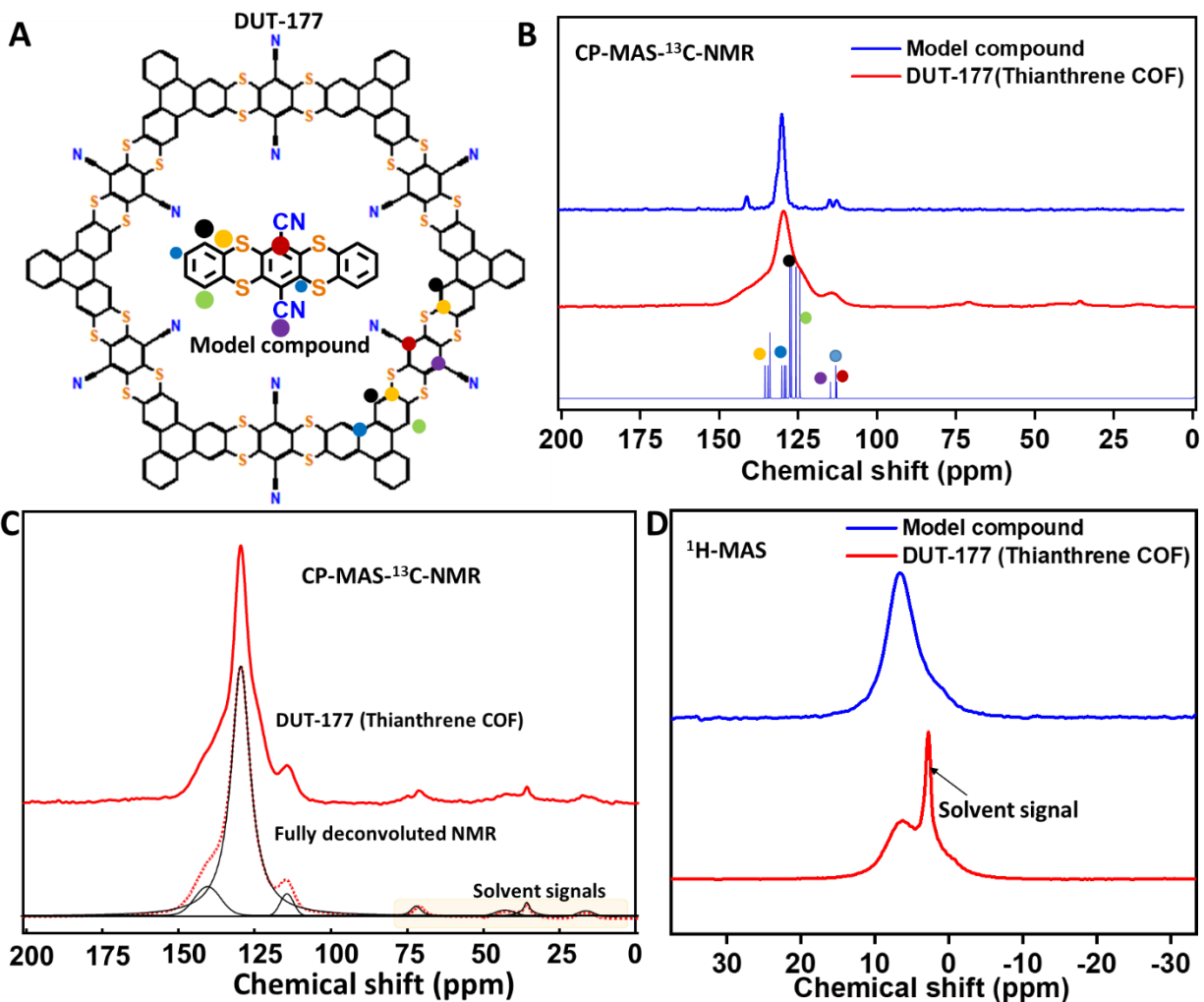


Figure S3. A. The chemical structure of DUT-177 and its model compound. The different type of carbon environment present in their structures. B. The comparison of the simulated CP-MAS- $^{13}\text{C}$ -NMR with the model compound and DUT-177. C. The deconvoluted CP-MAS- $^{13}\text{C}$ -NMR signals of DUT-177. D. The  $^1\text{H}$ -MAS NMR signals of DUT-177 and its model compound.

#### Solid-state NMR:

Figure S3 shows the full range CP-MAS- $^{13}\text{C}$ -NMR spectra of the DUT-177 and its model compounds including the simulated spectrum of the DUT-177 are shown. Simulation was carried out using ACD/Labs software. In general, DUT-177 and the model compound have similar signals in the aromatic region. Besides aromatic  $^1\text{H}$  signal, thiol  $^1\text{H}$  signal at 1.2 ppm and remnants solvent signal at 2.85 ppm are also observed for DUT-177. These minor signals appearing in the aliphatic region for the COF sample are mainly due to solvent remnants arising from the synthesis. Those solvent molecules are very strongly coordinated to the structure and provide CP signals even at short contact time in the  $^{13}\text{C}$  CP MAS NMR spectra (Fig.3). However, the signal from the loosely coordinated solvent to the structure disappear at short CP time.

#### Line broadening of the NMR signal:

The resolution and line width of the  $^{13}\text{C}$  spectra for the COF at 300 and 800 MHz spectrometers are very similar (data not shown). Therefore, the line broadening for DUT-177 can be due to two effects:

(i) A distribution of the isotropic chemical shift of the  $^{13}\text{C}$ -NMR signal. This phenomenon could be explained by the electron delocalization through the dithiine linking, which is also observed for the molecular orbital approximation (described in).

(ii) Another explanation for the line broadening might be anisotropy of the bulk magnetic susceptibility. COF materials having the layer type orientation could exhibit a strong anisotropy of the bulk magnetic susceptibility. For this reason, further line narrowing of the COF sample could not be possible. The line narrowing factor,  $\nu$  can be written as

$$\nu = \frac{\Delta\nu_{\frac{1}{2}}^{MAS}}{\Delta\nu_{\frac{1}{2}}^{Static}} = \frac{1}{3} \left| \frac{\Delta\chi}{\bar{\chi}} \right|, \text{ where } \Delta\chi = |\chi_{\perp} - \chi_{\parallel}| \text{ denotes the anisotropy and } \bar{\chi} = 1/3(2\chi_{\parallel} + \chi_{\perp}) \text{ is the isotropic average of the bulk magnetic susceptibility.}^{16}$$

Both effects, (i) and (ii) likely contribute to the pronounced line broadening observed for DUT-177.

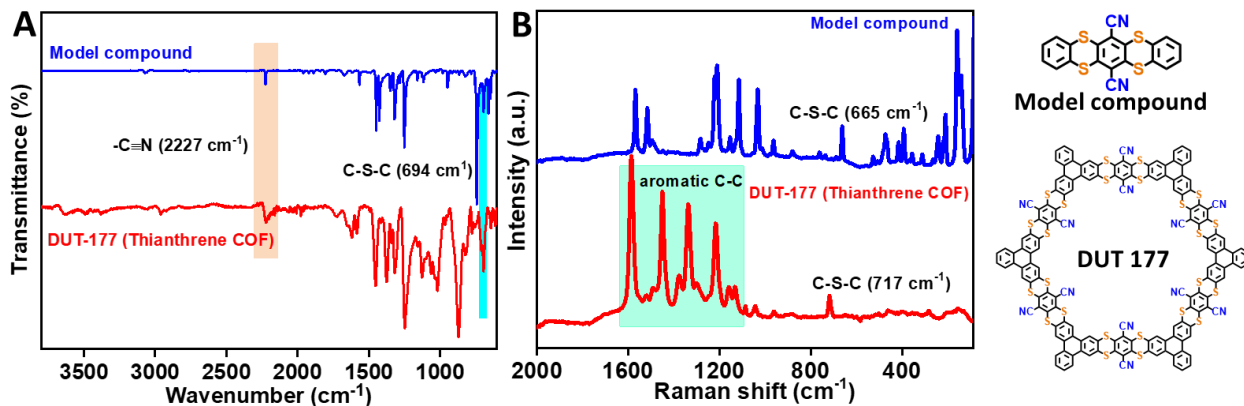


Figure S4. A. IR spectra of DUT-177 (red) and its model compound (blue). B. Raman spectra of DUT-177 and its model compound.

Table S2. Calculated and measured CHNS content of DUT-177 obtained from elemental analysis.

From unit cell				From elemental analysis			
N	C	H	S	N	C	H	S
6.99	59.98	1.01	32.02	6.45	53.40	2.21	38.30

#### IV. Structural modeling of DUT-177.

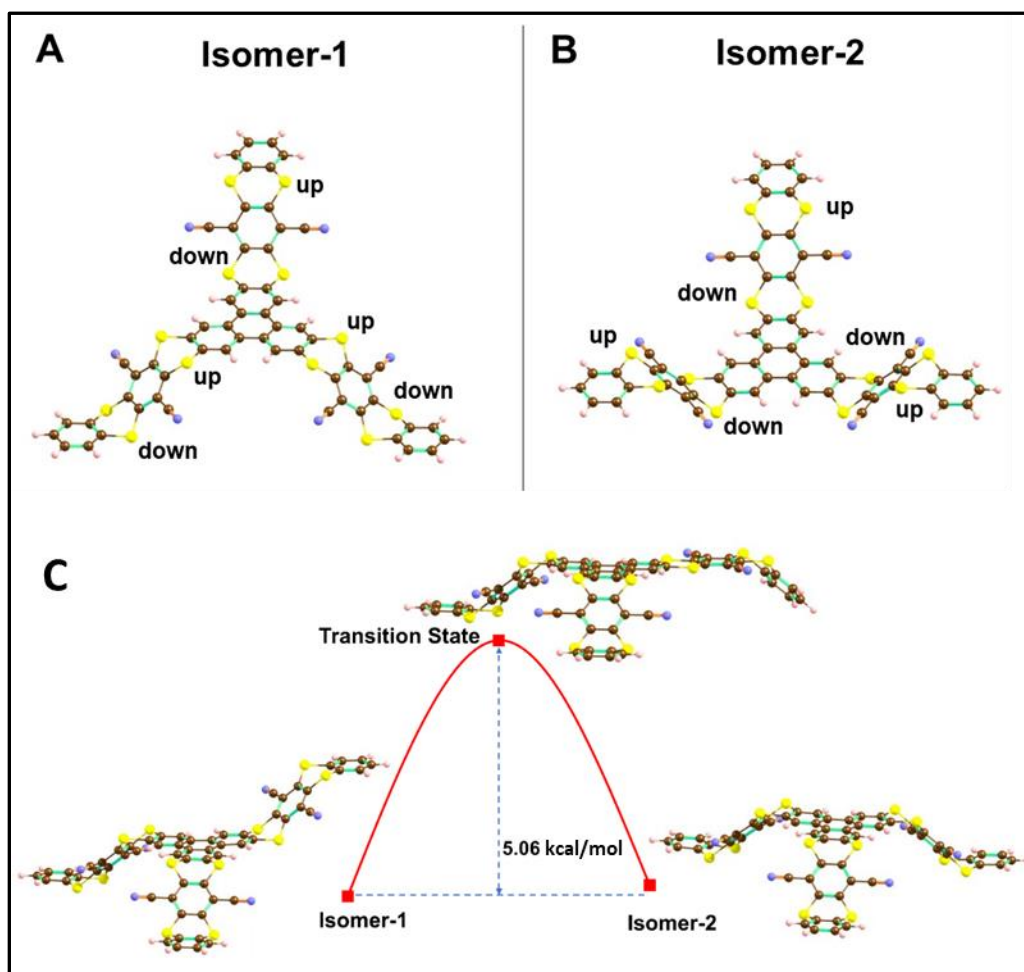


Figure S5. The possible molecular building units of DUT-177. A. Isomer-1. B. Isomer-2. C. The energy barrier profile for the transition of Isomer-1 to Isomer-2 via a transition state. The stabilization energy difference between these two isomers is very low (5.06 kcal mol<sup>-1</sup>). C, H, N and S are represented in brown, white, blue and yellow respectively.

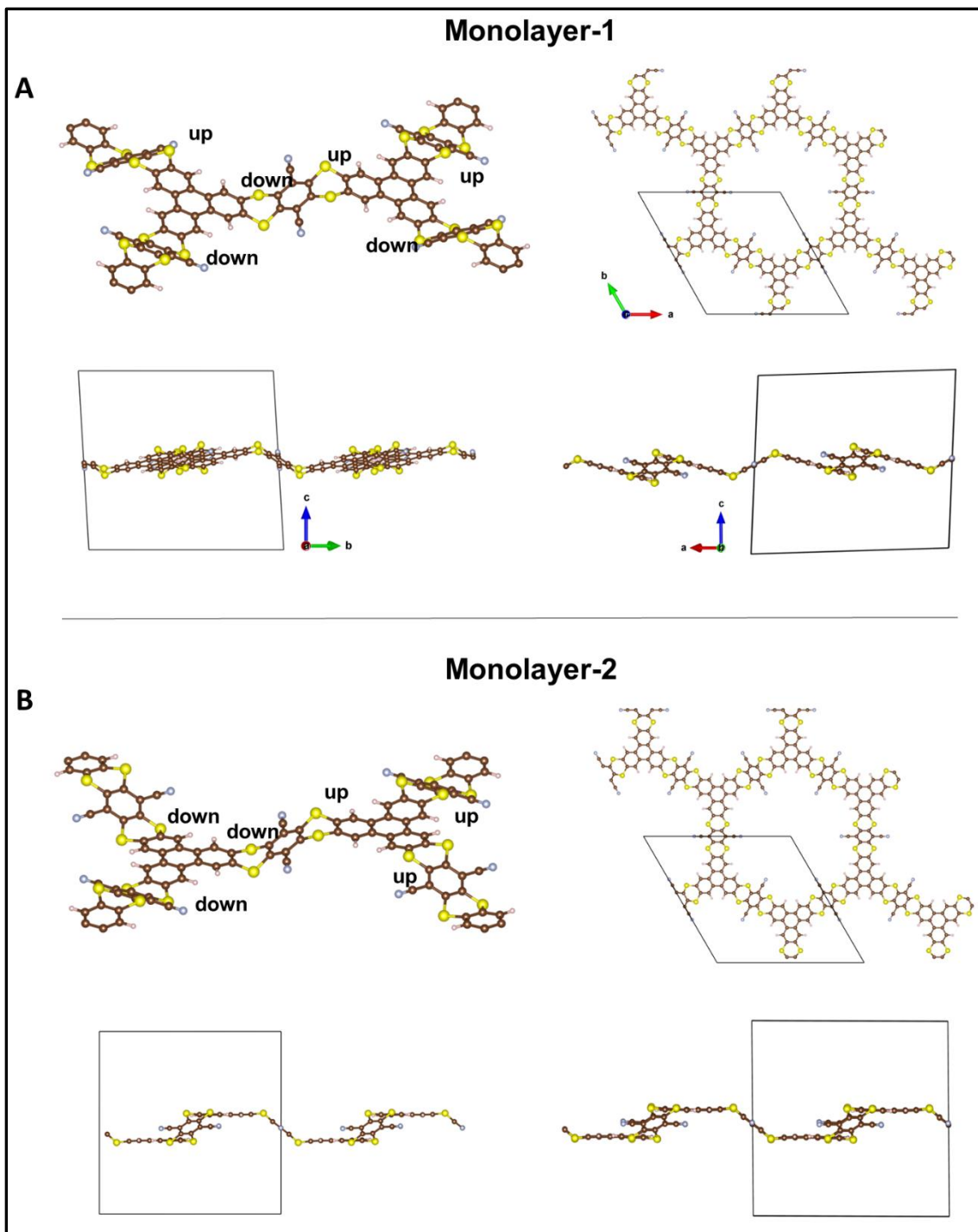


Figure S6. The monolayer of DUT-177 has two possible configurations which are generated from the two different isomers. A. Monolayer-1: The up-down configuration of thiathrene centers of DUT-177. B. Monolayer 2: The all up/all down configuration of thiathrene centers of DUT-177. C, H, N and S are represented in brown, white, blue and yellow respectively.

Table S3. The unit-cell parameters and relative energy difference of the two configurations of inclined structures.

Stacking	a (Å)	b (Å)	$\alpha^\circ$	$\beta^\circ$	$\gamma^\circ$	C-S-C ( $^\circ$ )	C-S bond (Å)	Relative energy difference (kcal/mol)
Configuration-1	25.86	25.36	91.57	92.76	119.24	101.47 - 102.14	1.577 - 1.762	0.00
Configuration-2	25.36	25.17	90.28	89.39	120.23	101.76 - 102.04	1.757 - 1.766	0.1

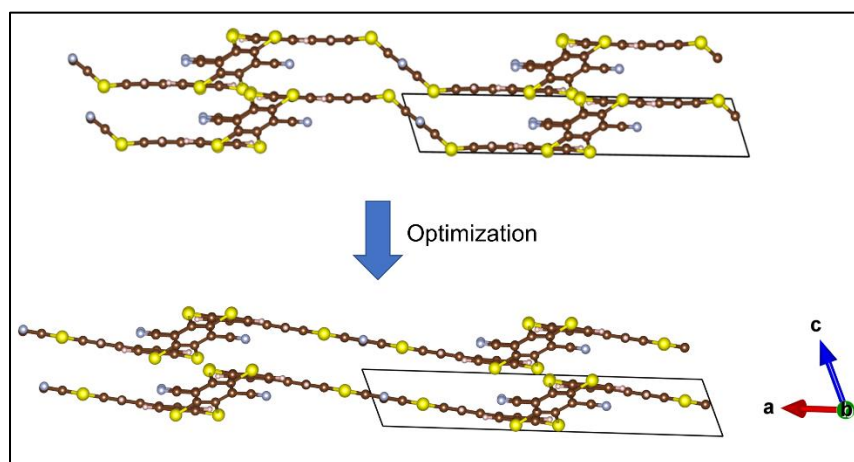


Figure S7. Structural optimization of layered form of monolayer-2 to local minima structure with one of the three thianthrene units being planar. C, H, N and S are represented in brown, white, blue and yellow respectively.

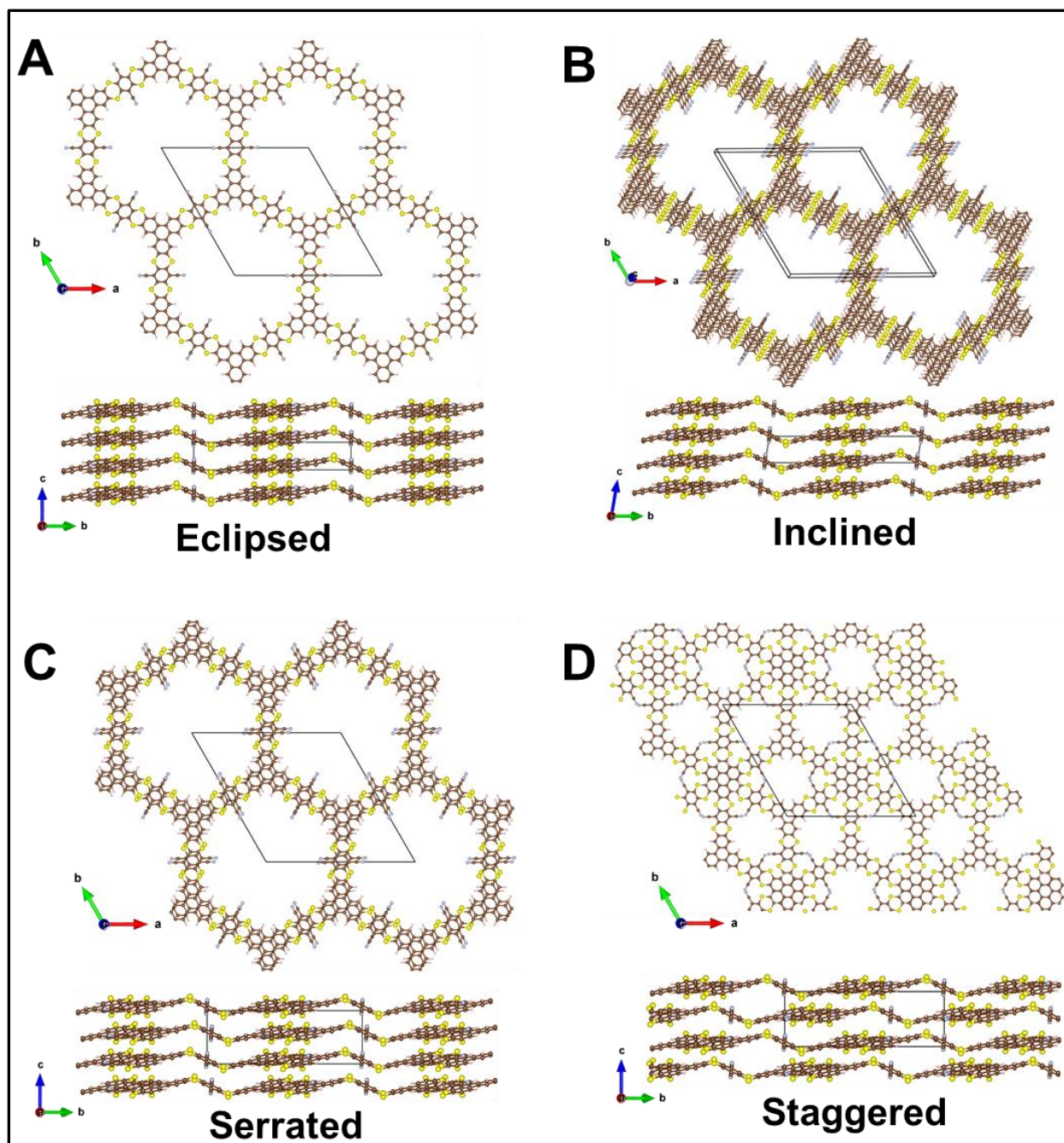


Figure S8. Different modelled structures of DUT-177 generated from monolayer-1 in different confirmations. A. Eclipsed. B. Inclined. C. Serrated. D. Staggered. The energy of the inclined stacking is the lowest. C, H, N and S are represented in brown, white, blue and yellow respectively.

Table S4. Unit-cell parameters and stacking energies of different conformers of DUT-177.

Stacking	$a$ (Å)	$b$ (Å)	$c$ (Å)	$\alpha^\circ$	$\beta^\circ$	$\gamma^\circ$	Stacking energy (kcal/mol)
Eclipsed	25.92	25.92	3.92	90	90	120	-61.6

Inclined	25.92	25.92	3.93	84.45	84.45	120	-64.4
Serrated	25.92	25.92	7.69	90	90	120	-61.4
Staggered	25.92	25.92	7.70	90	90	120	-32.5

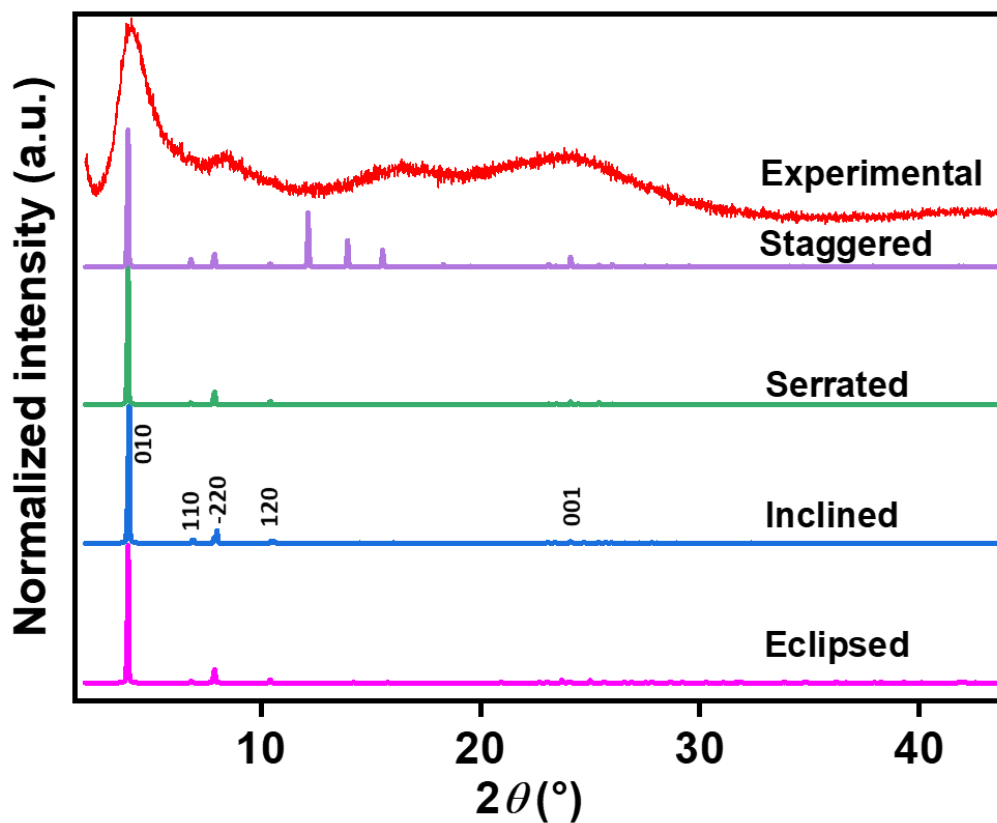


Figure S9. The simulated PXR D patterns of AA-eclipsed (magenta), AA-inclined (blue), AA-serrated (green) and AB-staggered (purple) stacking of DUT-177. These results show that the calculated PXR D patterns from AA-eclipsed, AA-inclined and AA-serrated stacking structures agree well with the experimental result. Besides, the DUT-177 with AA-inclined stacking structure shows higher energetic stability.

Table S5. Coordinates of atoms of the modeled structure (AA-inclined).

$a=b=25.92 \text{ \AA}$ ,  $c=3.93 \text{ \AA}$ ,  $\alpha=\gamma=84.45^\circ$ ,  $\beta=120^\circ$ ; Triclinic P1

Atoms	x	y	z
C	0.434602	0.992566	0.431151
C	0.163004	0.557565	0.284517
C	0.492521	0.045488	0.336607
C	0.556662	0.220862	0.298326
C	0.986297	0.382873	0.440084
C	0.490787	0.444273	0.374608
C	0.657801	0.269885	0.44784

C	0.986244	0.437022	0.4781
C	0.433697	0.438637	0.464149
C	0.554162	0.331674	0.340415
C	0.656364	0.379937	0.472826
C	0.98522	0.597736	0.566192
C	0.478756	0.936183	0.667578
C	0.36121	0.814681	0.683279
C	0.76075	0.320749	0.611669
C	0.412803	0.812444	0.744307
C	0.657952	0.21611	0.419431
C	0.587917	0.987737	0.6648
C	0.758974	0.426293	0.643759
C	0.655758	0.434296	0.456137
C	0.313768	0.711574	0.555886
C	0.414887	0.760833	0.705381
C	0.263423	0.604867	0.450668
C	0.480956	0.537439	0.640892
C	0.931937	0.487067	0.651224
C	0.313493	0.765314	0.583644
C	0.590811	0.595669	0.608914
C	0.21083	0.660371	0.392171
C	0.543808	0.043558	0.403453
C	0.380949	0.38604	0.406905
C	0.809625	0.369837	0.70483
C	0.543296	0.496807	0.417331
C	0.315369	0.601508	0.535015
C	0.262567	0.659194	0.46288
C	0.417634	0.650111	0.66682
C	0.039048	0.547056	0.376547
C	0.808681	0.423393	0.722015
C	0.366835	0.653846	0.604107
C	0.427469	0.938094	0.600503
C	0.315929	0.547097	0.555657
C	0.364424	0.543097	0.64761
C	0.605878	0.272347	0.38476
C	0.932568	0.433639	0.629279
C	0.416711	0.595849	0.695228
C	0.604914	0.327775	0.401863
C	0.383286	0.993963	0.340754
C	0.212806	0.554872	0.363215
C	0.039703	0.493626	0.355051
C	0.428444	0.484853	0.59897

C	0.161973	0.611112	0.300219
C	0.709056	0.3221	0.541649
C	0.365761	0.709264	0.619246
C	0.985361	0.54365	0.527807
C	0.558614	0.169196	0.2589
C	0.536645	0.989123	0.573513
C	0.538051	0.54305	0.551918
C	0.610174	0.166852	0.319485
C	0.708295	0.37644	0.555697
C	0.555045	0.385901	0.315891
C	0.60727	0.438482	0.365927
H	0.27697	0.505971	0.509176
H	0.20807	0.70066	0.407684
H	0.458721	0.689989	0.705246
H	0.211865	0.512557	0.353876
H	0.515887	0.220938	0.253777
H	0.696401	0.212154	0.472515
H	0.513108	0.291938	0.300263
H	0.694681	0.475252	0.504593
H	0.274968	0.769121	0.530414
H	0.76345	0.280457	0.59481
H	0.455684	0.760856	0.75053
H	0.760037	0.468644	0.654016
N	0.633154	0.638238	0.669068
N	0.986612	0.338999	0.397441
N	0.342348	0.995464	0.24981
N	0.98487	0.641572	0.609355
N	0.338634	0.343477	0.346471
N	0.628767	0.98618	0.756756
S	0.491876	0.385832	0.189466
S	0.101345	0.61862	0.194606
S	0.617666	0.104547	0.255139
S	0.616416	0.510758	0.284886
S	0.47406	0.871427	0.888663
S	0.868047	0.486676	0.850706
S	0.49726	0.110234	0.115036
S	0.353598	0.876945	0.74725
S	0.479811	0.596031	0.823945
S	0.103701	0.494067	0.156844
S	0.355343	0.470882	0.732436
S	0.870145	0.362076	0.810009

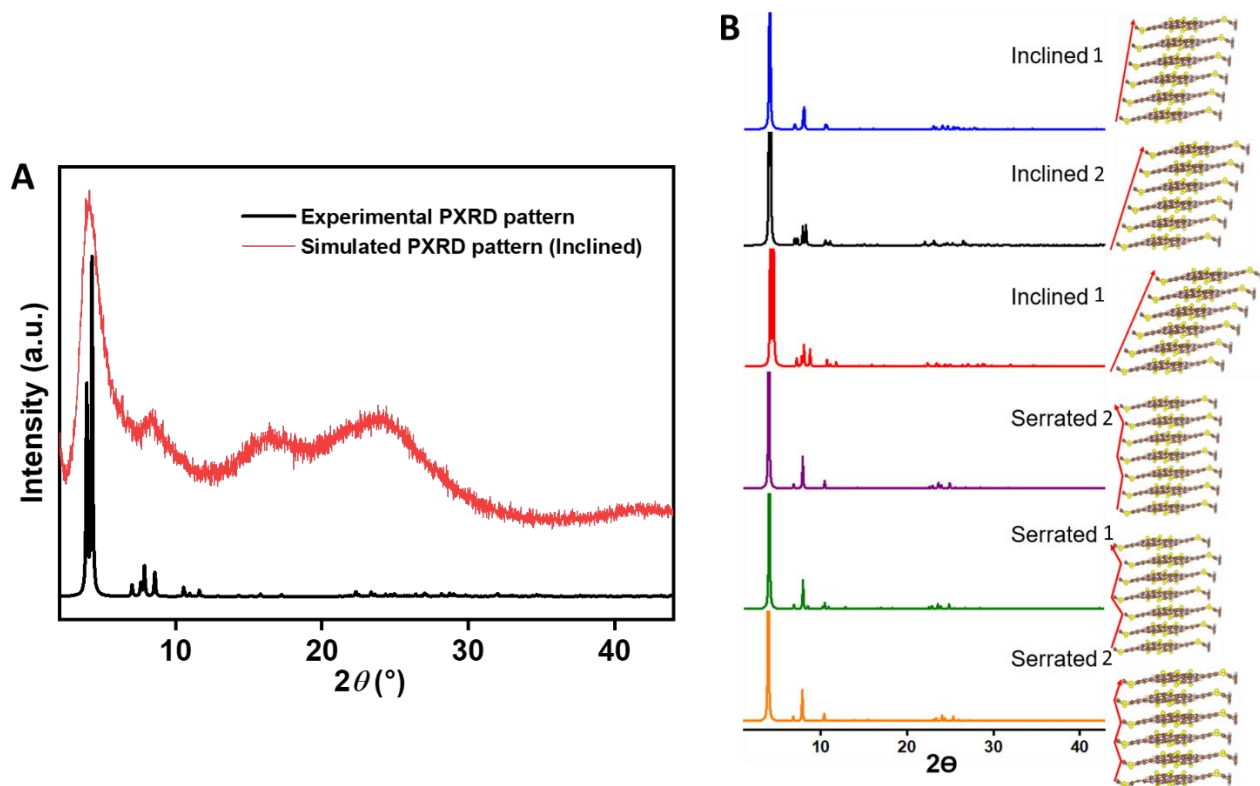


Figure S10. A. Fitting of the simulated PXRd pattern of DUT-177 in its AA-inclined 2 model with the experimentally obtained pattern. B. Pictorial representation of different slipped layered structures of DUT-177 with varying extent of offsets.

## V. FESEM and HRTEM Imaging of DUT-177.

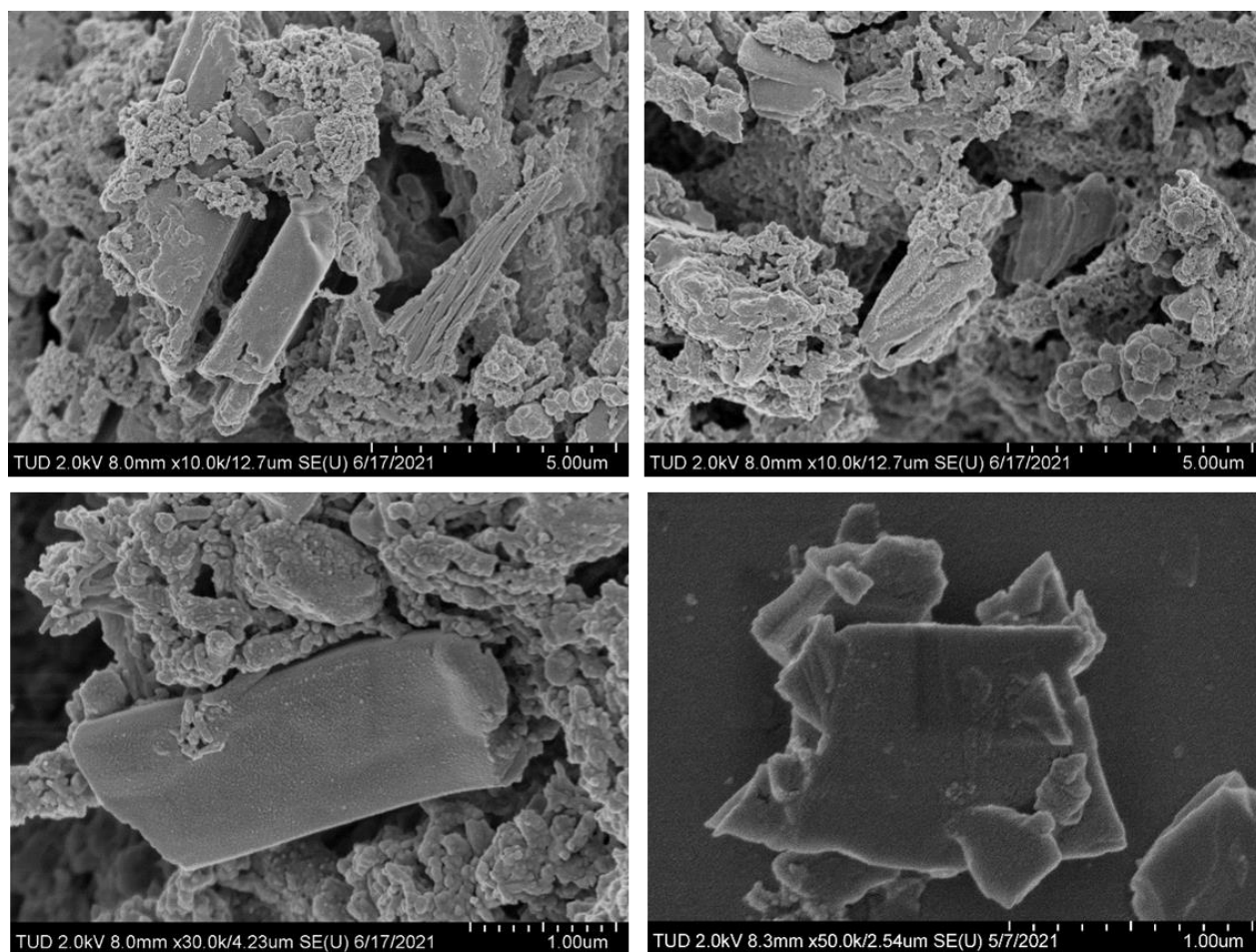


Figure S11. (i). The FESEM images of the DUT-177 at different magnifications (on powdered sample without prolonged sonication).

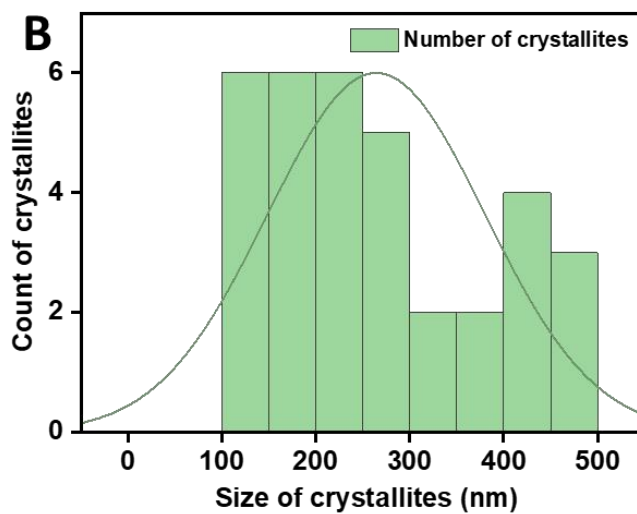
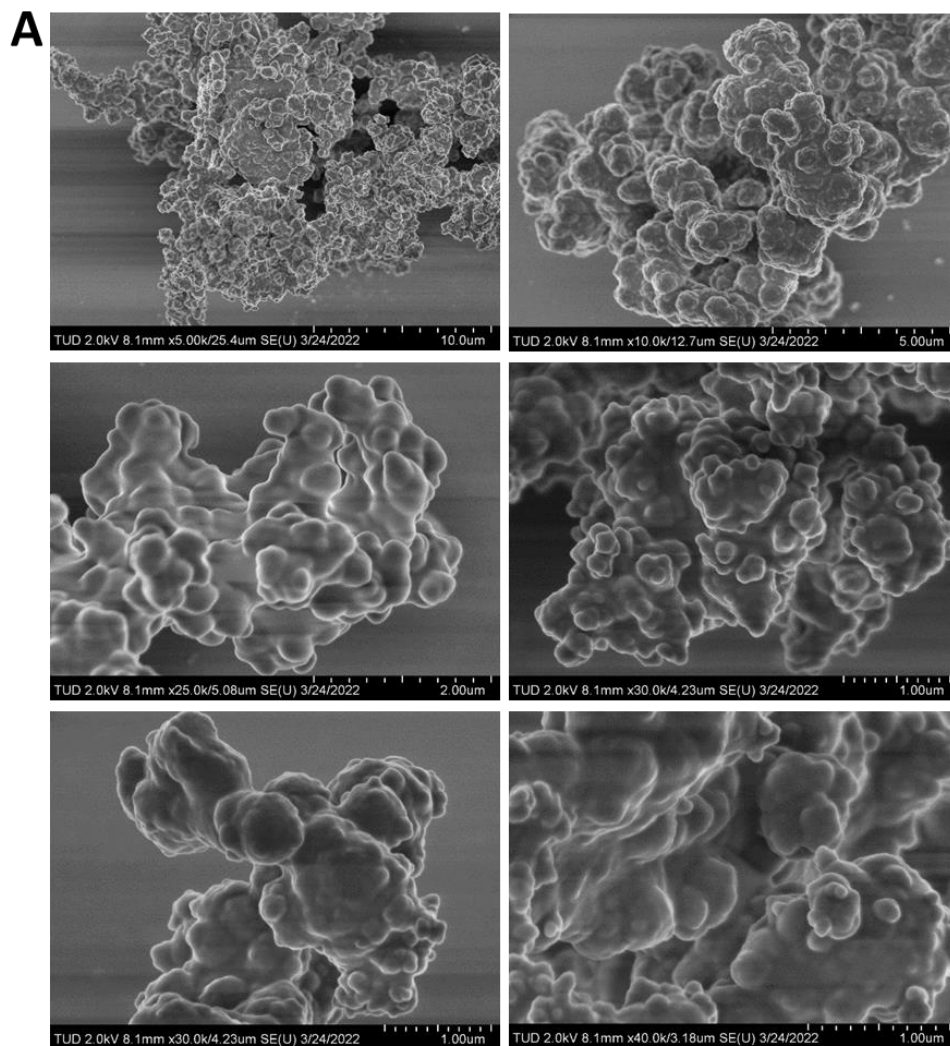


Figure S11. (ii). A. The FE-SEM images of the DUT-177 at different magnifications (after prolonged sonication assisted dispersion in ethanol). B. The particle size distribution of DUT-177 based on the coagulated particles observed in FE-SEM. No homogeneous distribution was obtained.

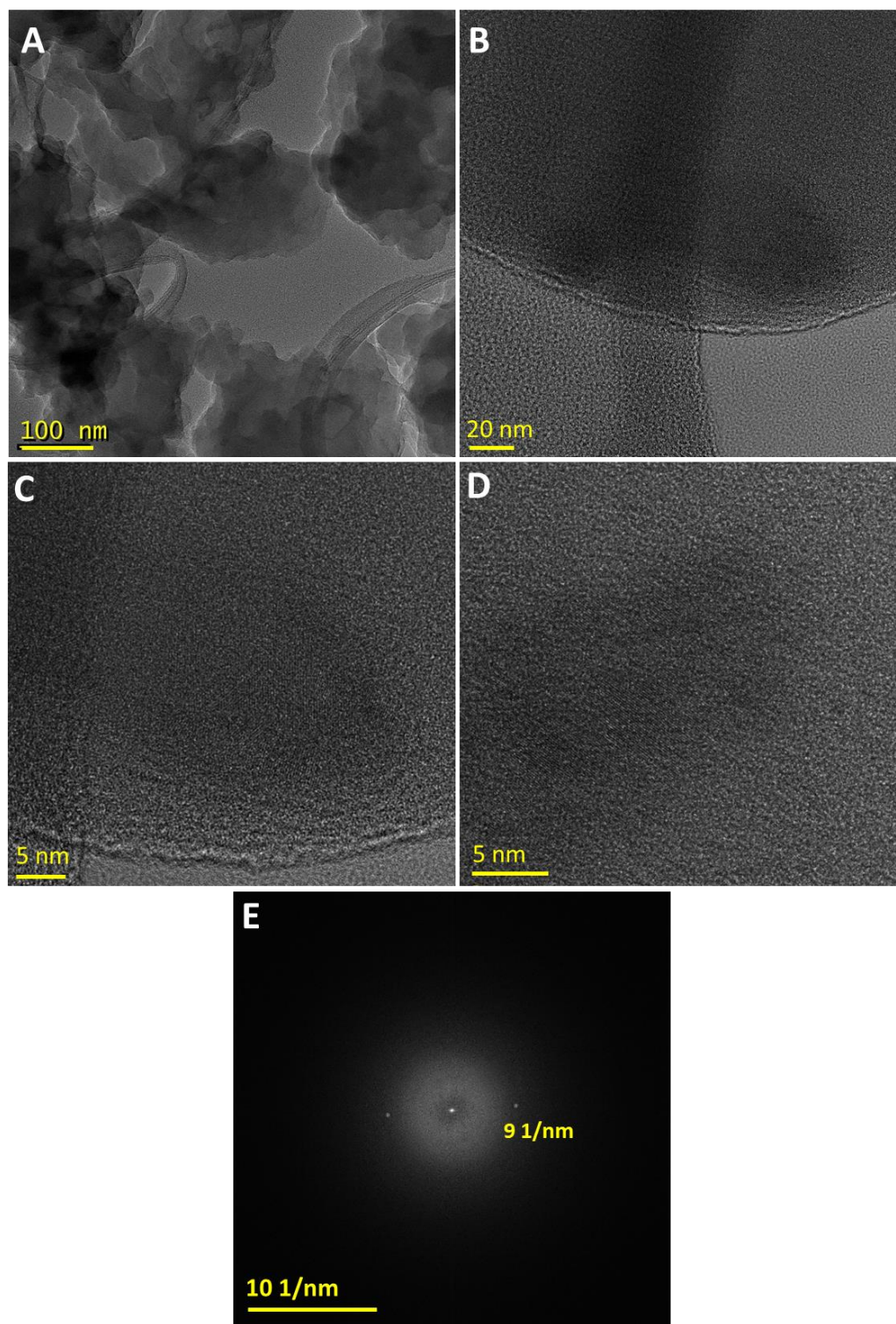


Figure S12. A, B, C, D. HRTEM micrographs of DUT-177 at different magnification (after prolonged sonication assisted dispersion in ethanol). Lattice fringes were not prominent due to very low crystallinity. The d-spacing of approximately 0.38 nm were obtained on most of the COF flakes. E. The FFT image of DUT-177.

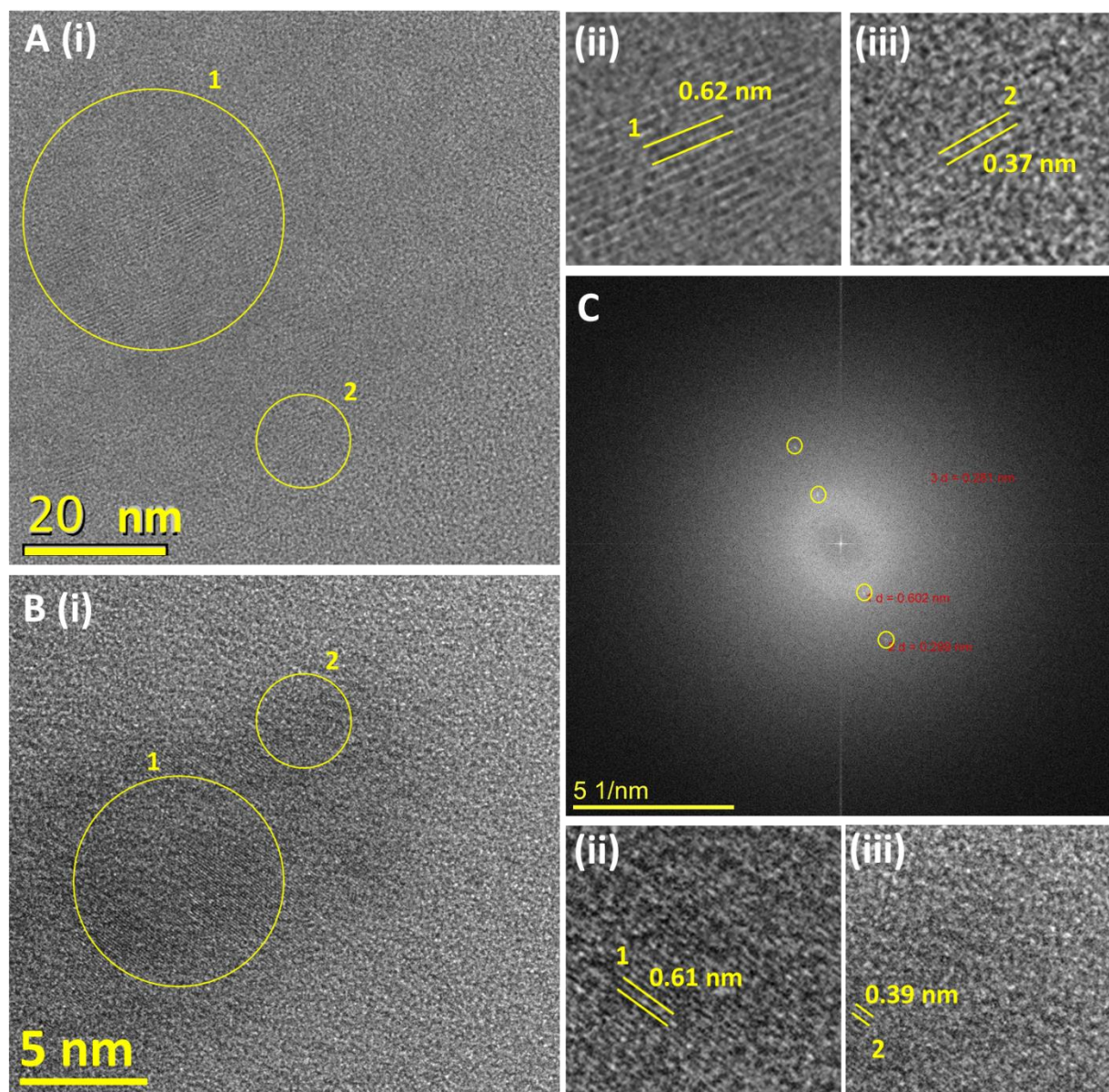


Figure S13. A (i) and B (i). The short range order of the lattice fringes of the flakes of DUT-177. A (ii) and B (ii). The zoomed area of the fringes. C. The SAED pattern of the crystalline COF showing the d-spacing.

## VI. Adsorption data analysis.

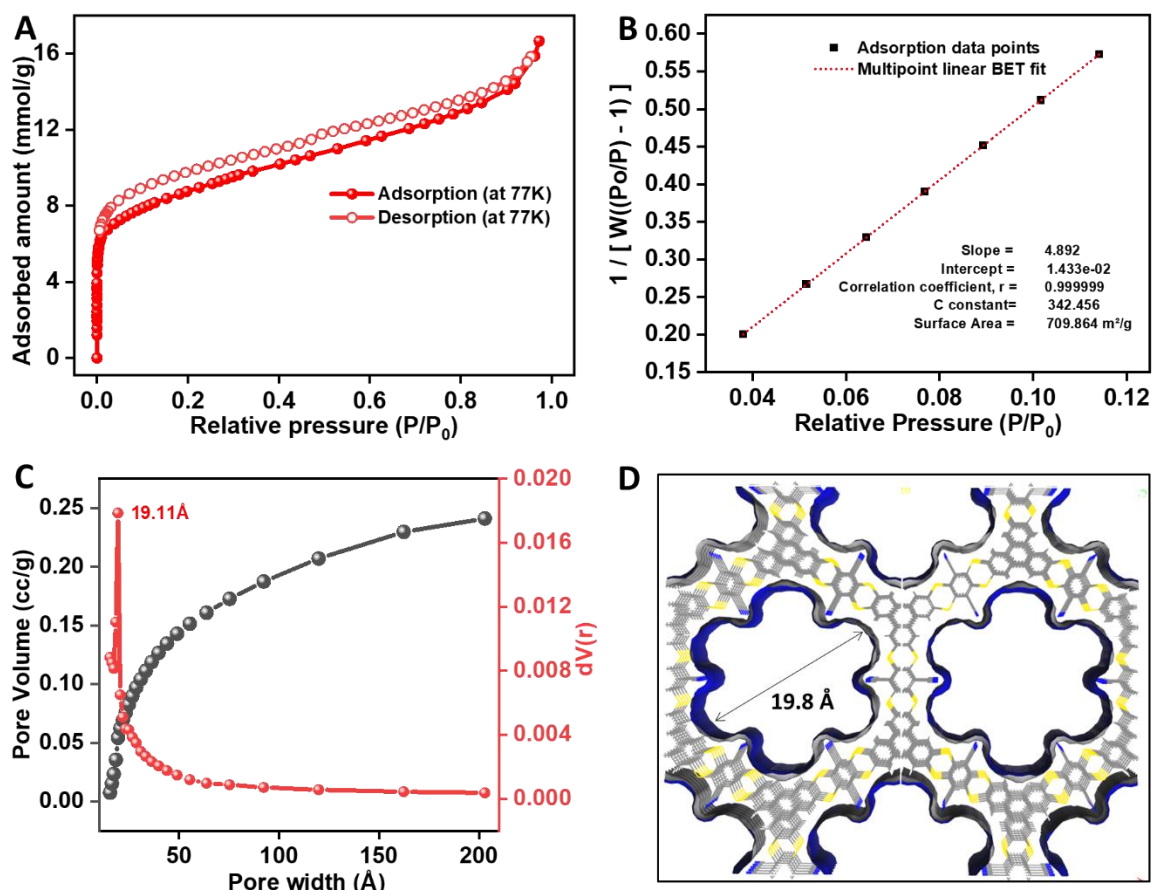


Figure S14. A. N<sub>2</sub> Physisorption isotherms of DUT-177 at 77K; filled symbols represent adsorption branch, empty symbols desorption. B. BET fitting of adsorption isotherm of N<sub>2</sub> at 77K. C. BJH fitting of the N<sub>2</sub> desorption isotherms at 77K was used for the determination of the pore width and pore volume distribution. D. The connolly surface of DUT-177 showing the pore-dimension.

VII. Electronic energy level calculations and band structure analysis of DUT-177.

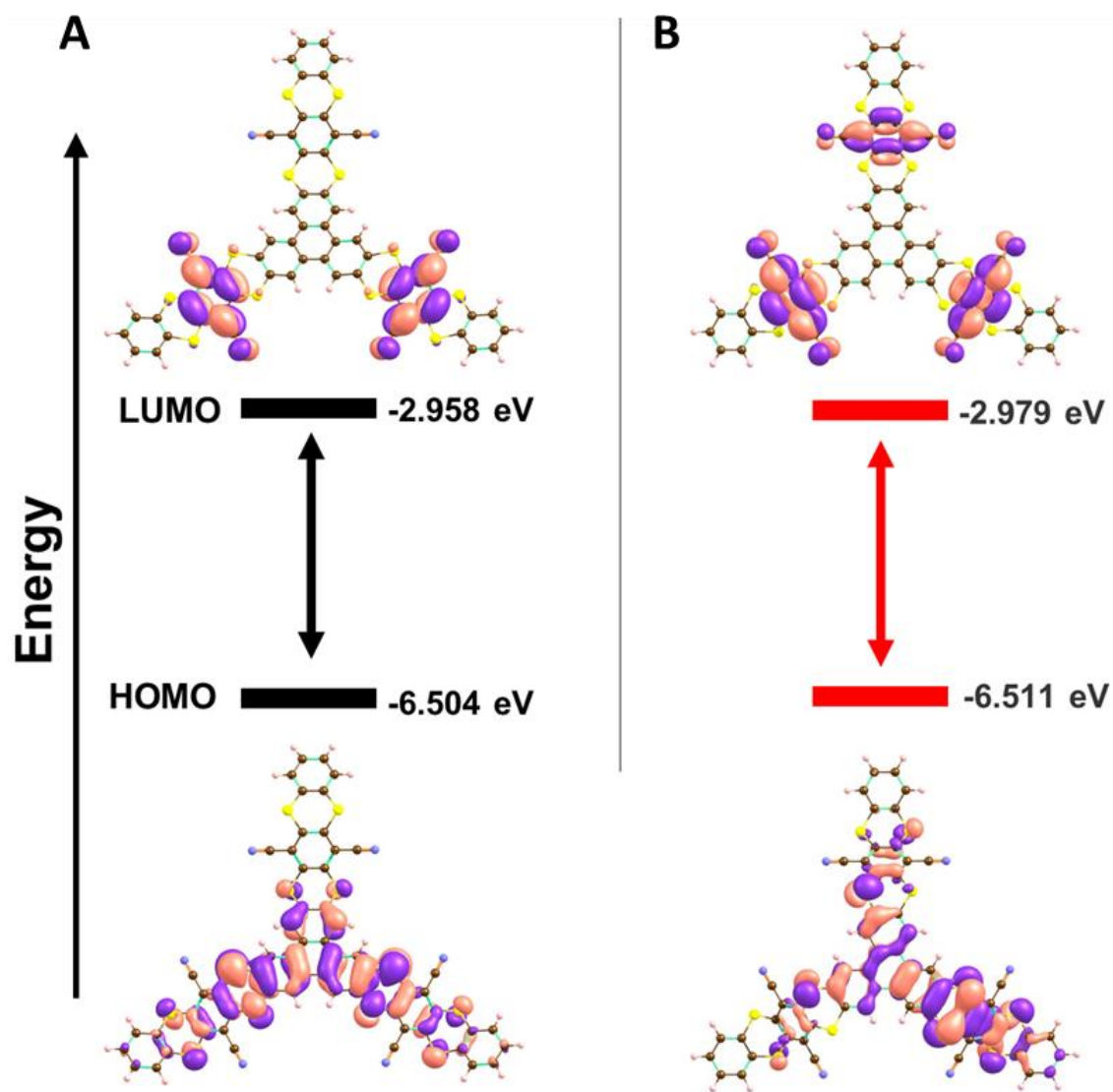


Figure S15. The position of HOMO and LUMO on the molecular unit of the DUT-177 in A. isomer-1 and B. isomer-2.

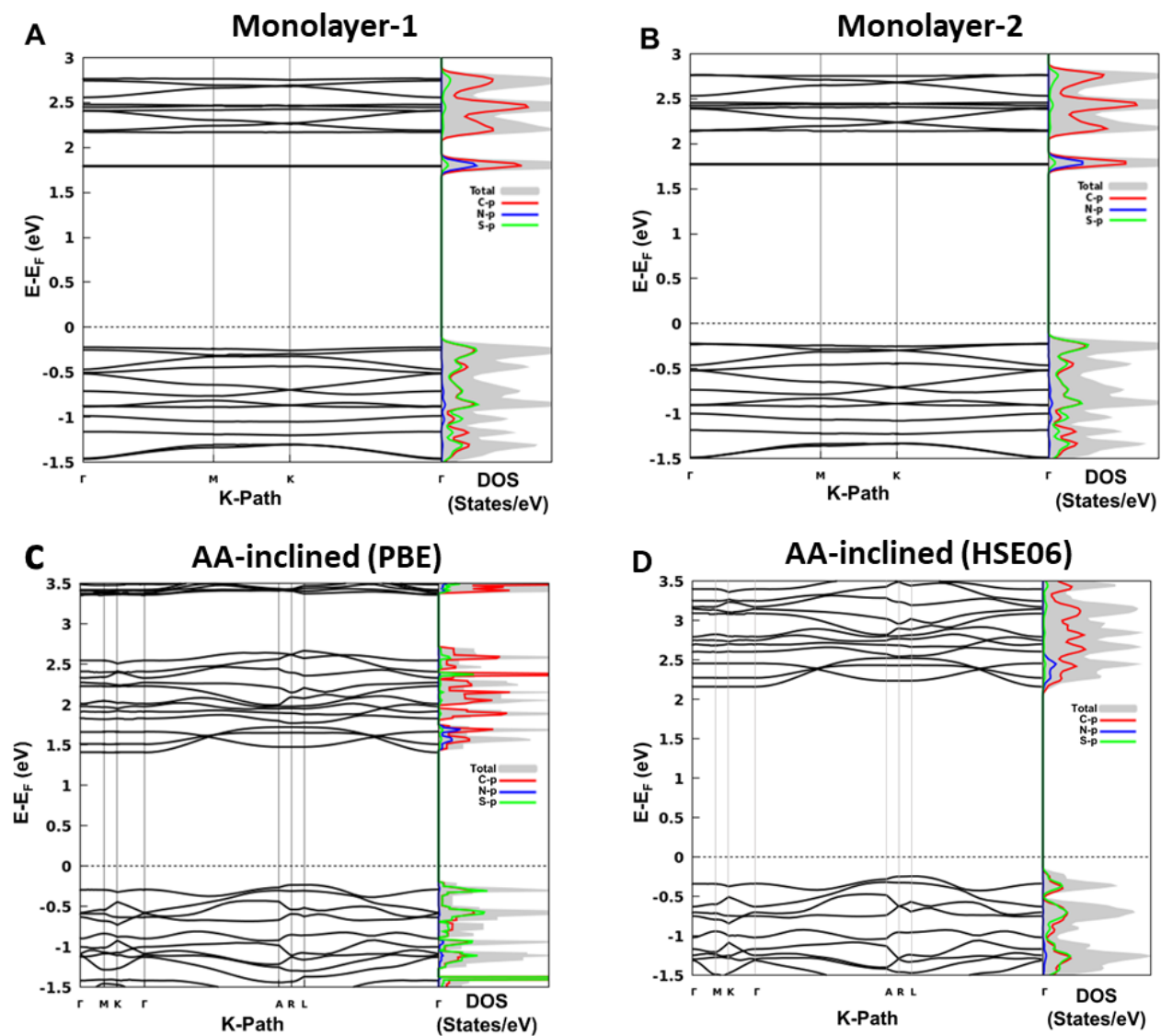


Figure S16. PBE band structures of (A) monolayer-1 (2.01 eV) and (B) monolayer-2 (1.99 eV) of DUT-177. Electronic band structure analysis of AA-inclined stacking (configured from stacking of monolayer-1) of DUT-177 calculated using (C) PBE functional (1.62 eV) and (D) HSE06 functional (2.45 eV).

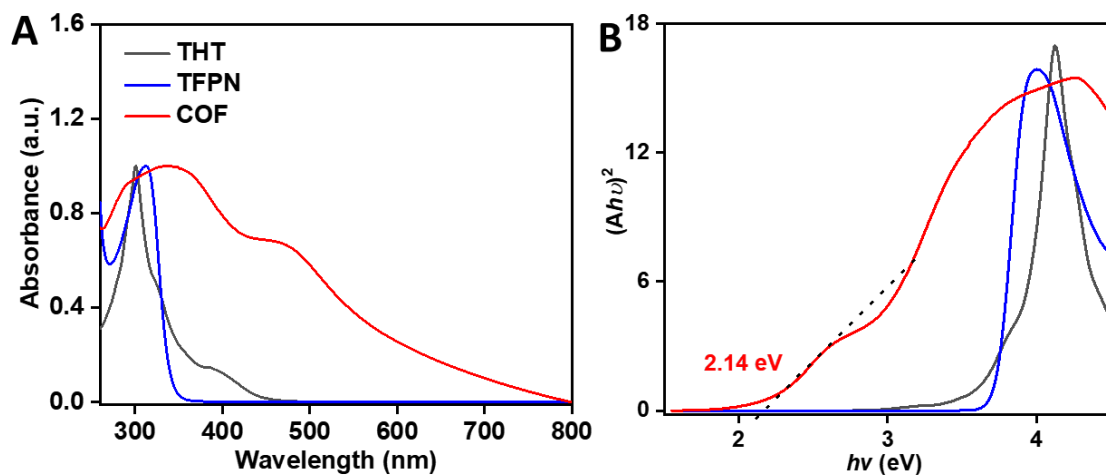


Figure S17. A. Comparison of the UV-Vis spectra of the monomers (THT, TFPN) with DUT-177 (red). B. The 'Tauc' plots extracted from the UV-Vis spectra.

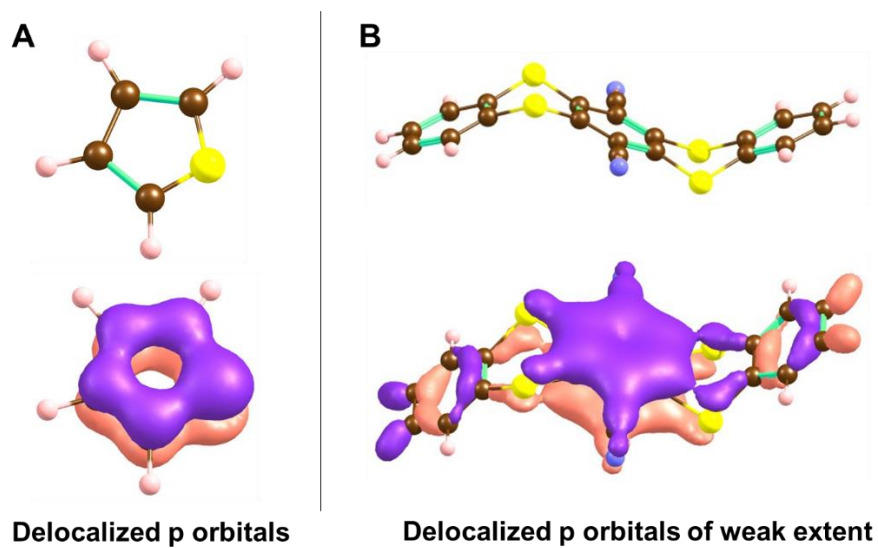


Figure S18. A. The complete delocalization of electronic cloud of p orbitals of carbon and sulfur in a thiophene molecule. B. The partial delocalization of the electronic cloud of p orbitals of carbon and sulfur in a thianthrene molecule.

### VIII. Cyclic Voltammogram of DUT-177 derived coin-cell.

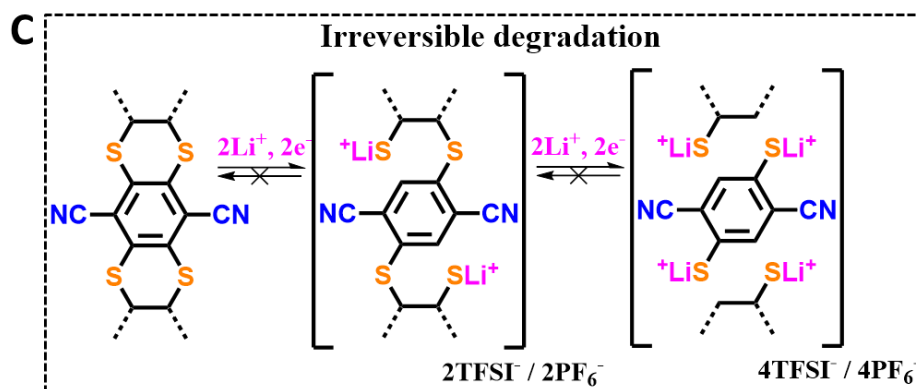
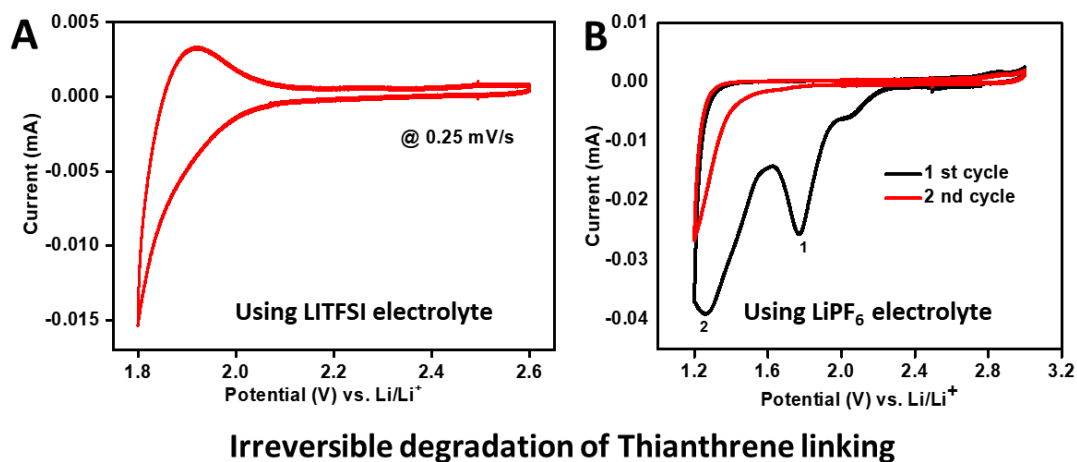


Figure S19. A. The CV of DUT-177 derived coin-cell using LiTFSI in DOL : DME (1:1) electrolyte (40  $\mu$ L). B. The CV of DUT-177 derived coin-cell using LiPF<sub>6</sub> in EC : DMC (1:1) electrolyte (40  $\mu$ L). C. Suggestion of a plausible pathway of irreversible degradation of dithiine linkage upon Lithium interactions.

### IX. Characterization of model compound before and after sulfurization.

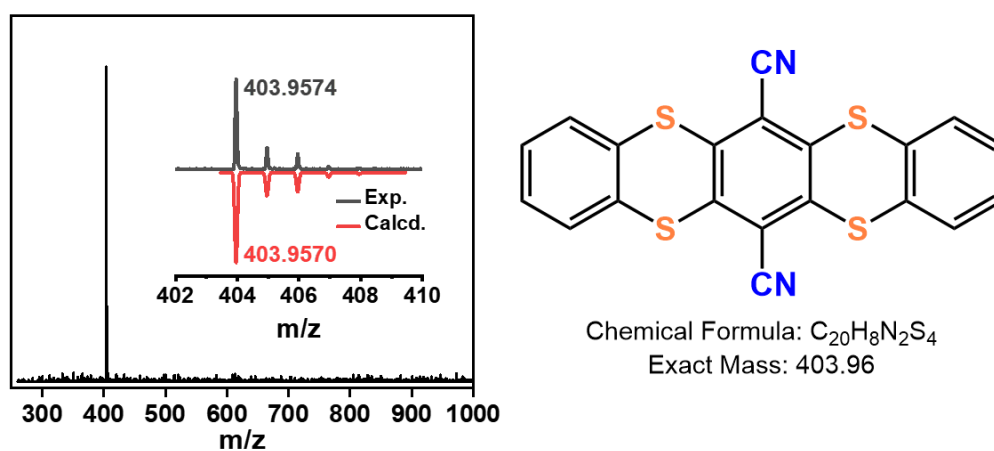


Figure S20. Comparison of the experimentally obtained mass spectra (analyzed by MALDI-TOF) of the model compound with the theoretical one.

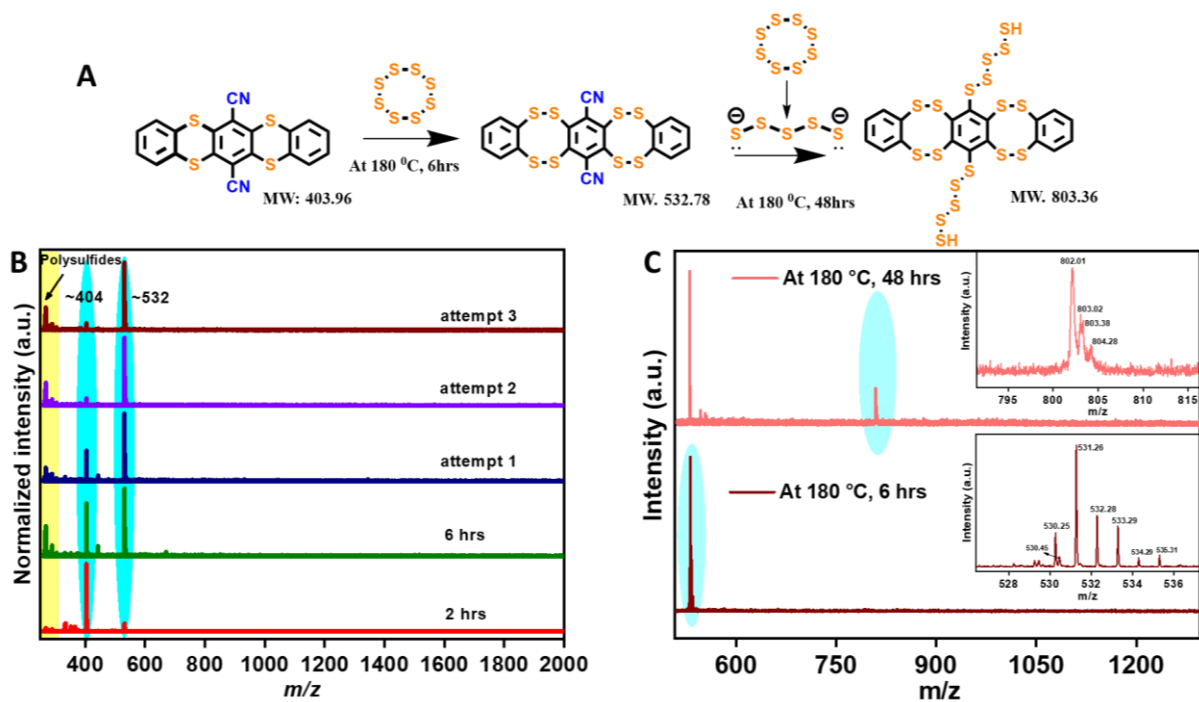


Figure S21. A. A plausible sulfurized form of the model compounds at different intervals of the sulfurization procedure and their corresponding masses. B. MALDI-TOF-MS data of the sulfurized model compounds. Appearance of a new mass was observed at around  $m/z=532$  at most of the attempts of the sulfurization. C. MALDI-TOF-MS data after prolonged sulfurization. This leads to possible substitution of the nitrile groups of the model compound by polysulfides along with the appearance of the new peak at  $m/z=802.01$ . (Inset) Fragmentation of the mass of the corresponding compounds obtained in High resolution mass spectrometry using MALDI-TOF technique.

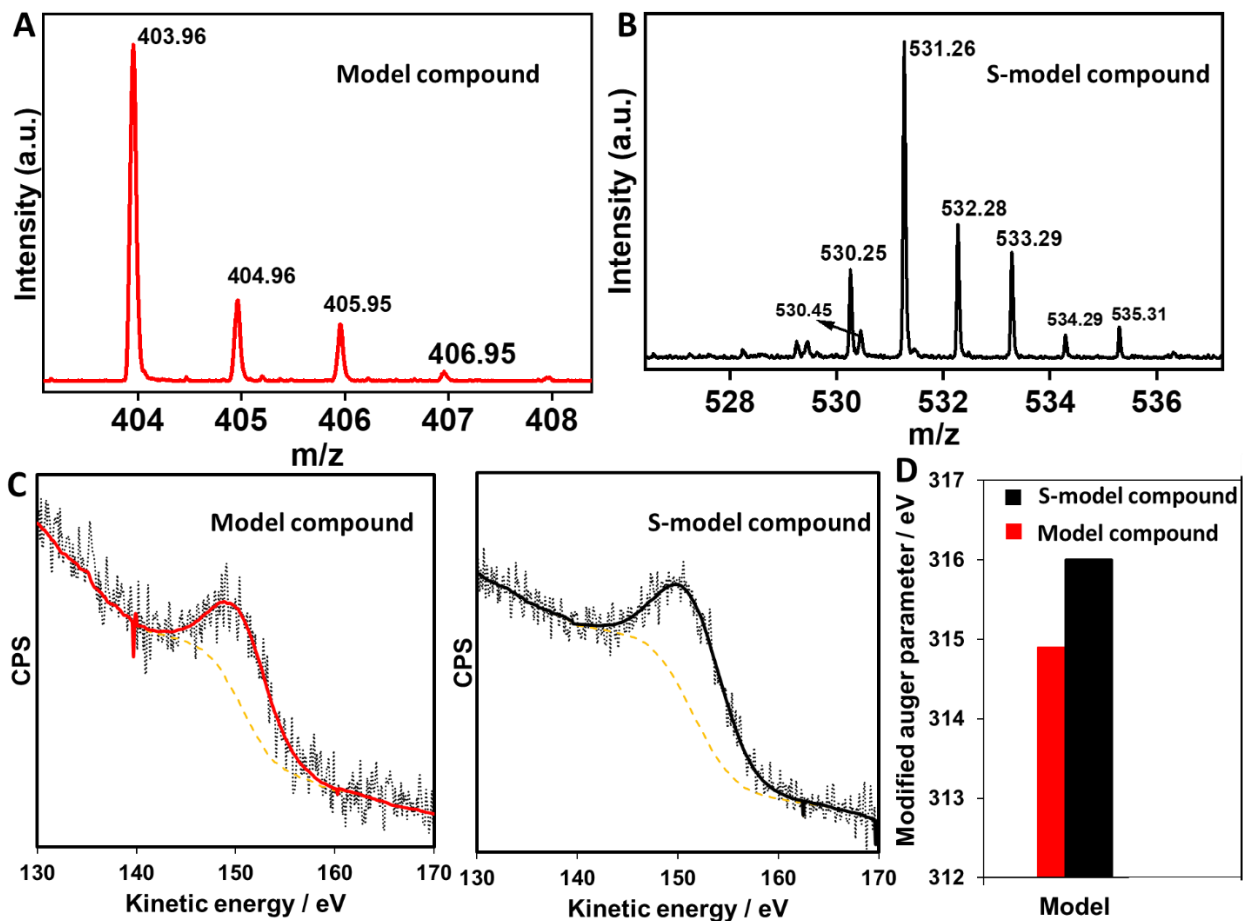


Figure S22. A and B. The high resolution mass spectra obtained from the MALDI-TOF-MS analysis showing the fragmentation pattern of the model compound and S-model compound. C. Auger Electron Spectroscopy (AES) data of model compound and S-model compound. Measurement points are shown in grey, fit in red and black and background in yellow. C. The modified Auger parameter ( $a'$ ) of the model compound and S-model compound.

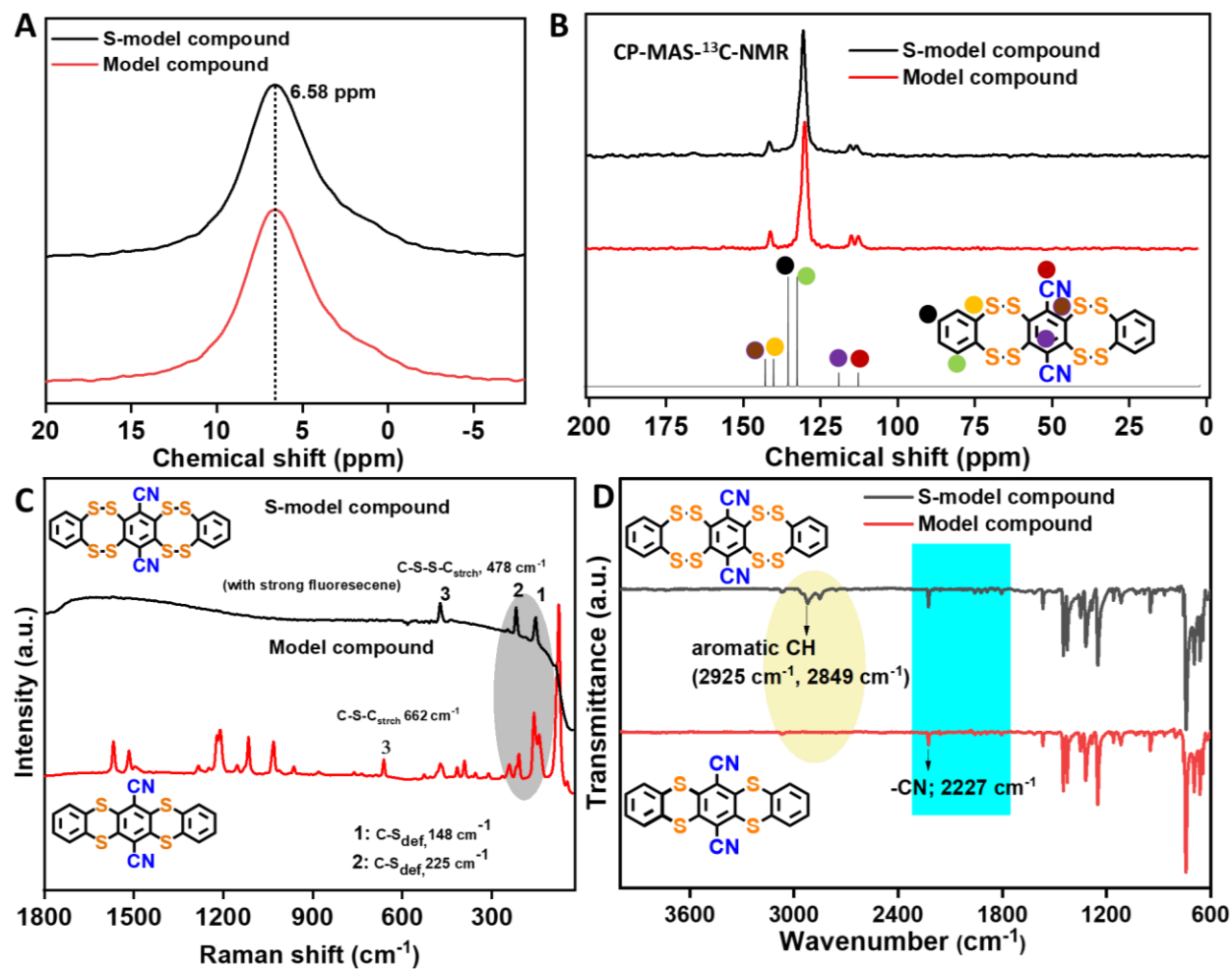
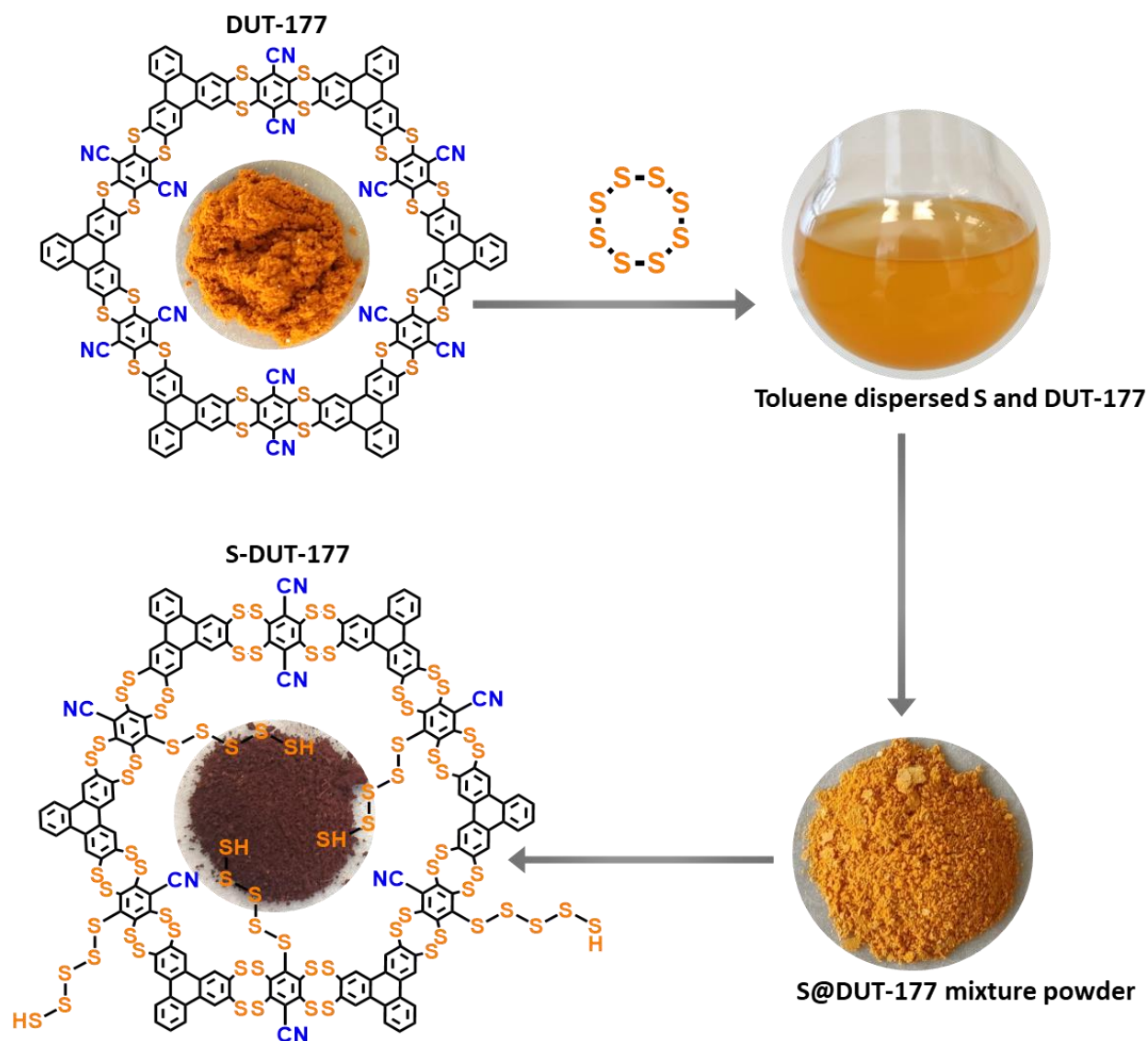


Figure S23. A. The  $^1\text{H}$ -MAS NMR signals of the model compound before and after sulfurization (S-model compound). B. Comparison of the simulated CP-MAS- $^{13}\text{C}$ -NMR with the sulfurized model-compound and the pristine model compound. C. Comparison of the Raman-shifts of the model compound with the S-model compound. The strong fluorescence background of the S-model-compound suppresses most of the characteristics signals. Only the signals related to the sulfur are obtained after applying the high power of the Laser beam. D. IR stretching frequencies of the model compound and the S-model-compound. Because of the similarity in the functional groups no distinguishable change is detected except for the intensification of the aromatic CH vibrations.

## X. Synthesis and Characterization of S-DUT-177 (Sulfurized DUT-177).



Scheme S3. The procedure for conversion of DUT-177 to S-DUT-177 by sulfurization.

### Synthesis of S-DUT-177

Elemental sulfur (250 mg, 7.8 mmol) was dissolved in toluene and activated powder of DUT-177 (50 mg) was dispersed in the sulfur. The weight ratio of sulfur to COF was 5:1. Afterwards, the excess solvent was removed in vacuo and the resulting S@COF was ball milled for 1 hour to ensure close contact of the COF with the sulfur. Next the obtained S@COF material was placed inside a quartz ampoule which was flame sealed under vacuum at  $10^{-3}$  Torr. The sealed ampoule was subjected to a temperature program inside of a tubular furnace. First the ampoule was kept at 120 °C for 2 hours, afterwards at 150 °C for 6 hours and finally at 360 °C for 12 hours. A red-brown product was obtained, which was thoroughly washed by solvent exchange with toluene to remove unreacted sulfur from the material. Finally, the obtained material was dried at elevated temperatures and stored in an argon filled glovebox until further manipulation. Elemental analysis: C: 14.76 %; H: 0.18 %; N: 0.89 % and S: 85.69 %. Yield: 78 mg.

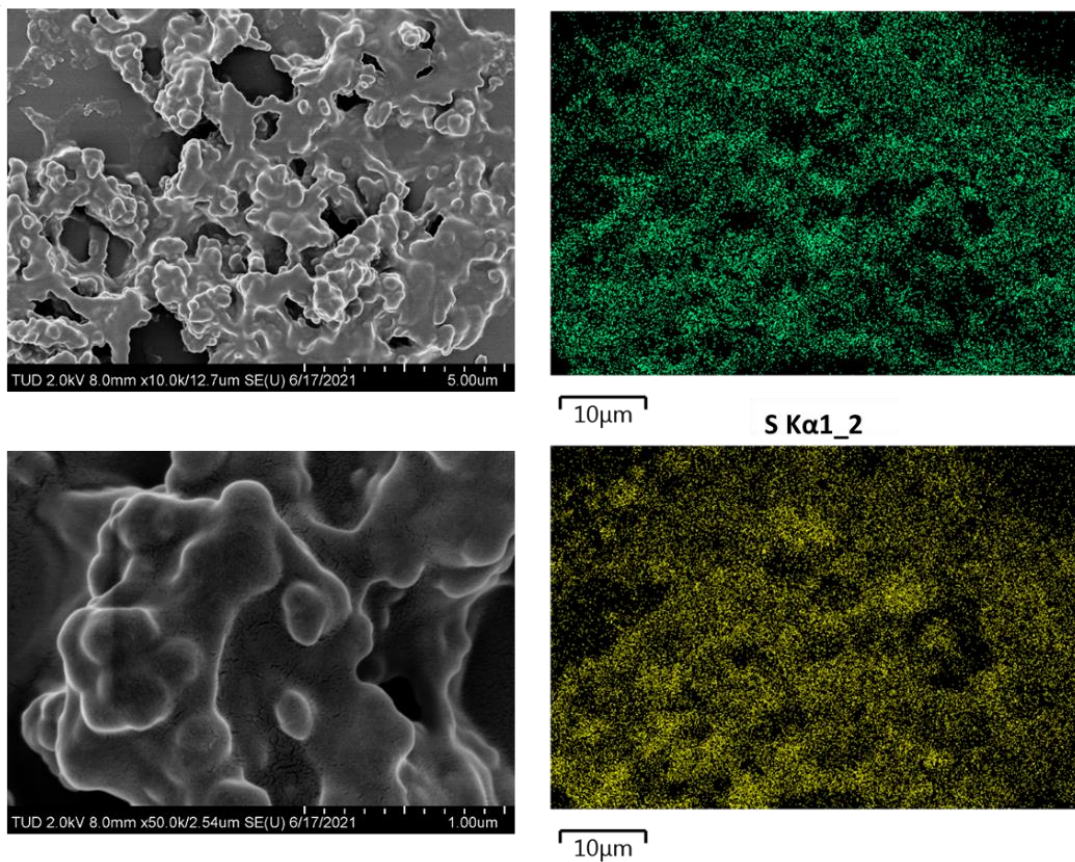


Figure S24. SEM and EDAX analysis on S-DUT-177. The EDAX analysis on S-DUT-177 shows that the carbon skeleton of the framework is fully sulfurized.

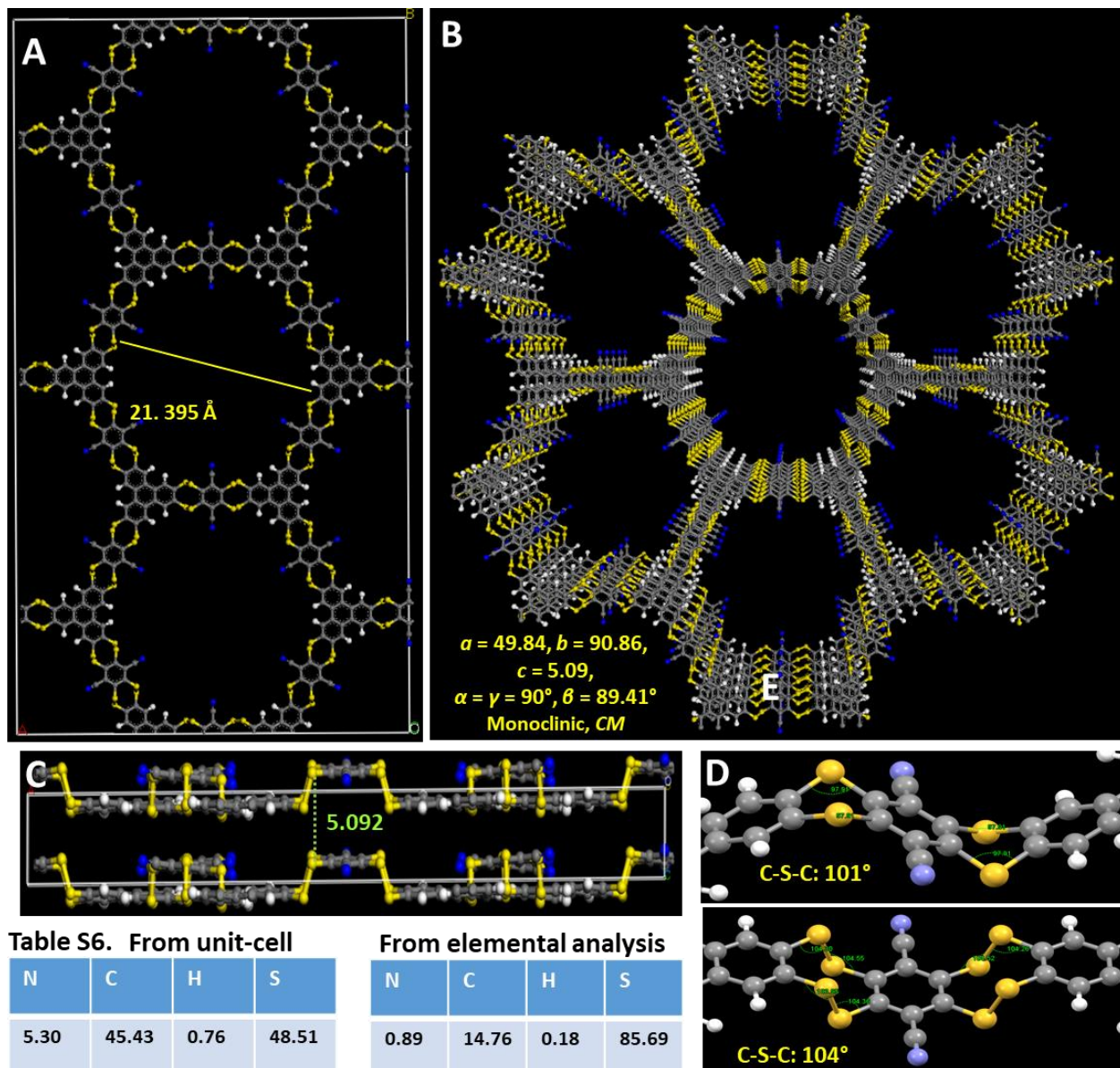


Figure S25. A. Possible unit cell of S-DUT-177 from the structural modeling. (Below) the unit-cell parameters. B. 3D view of 2D-dithianthrene based framework. C. The enhanced dihedral angle along sulfur-sulfur linkage and enhanced inter layer distance. D. Comparison of bending of the layers of DUT-177 and S-DUT-177 along the sulfur centers.

Table S6. CHNS percentage of S-DUT-177.

N.B. Presence of excess amount of sulfur was noticed in the sulfurized DUT-177. This suggests the thianthrene to dithianthrene conversion cannot be the only possible sulfurization of the framework. There could be other side reactions.

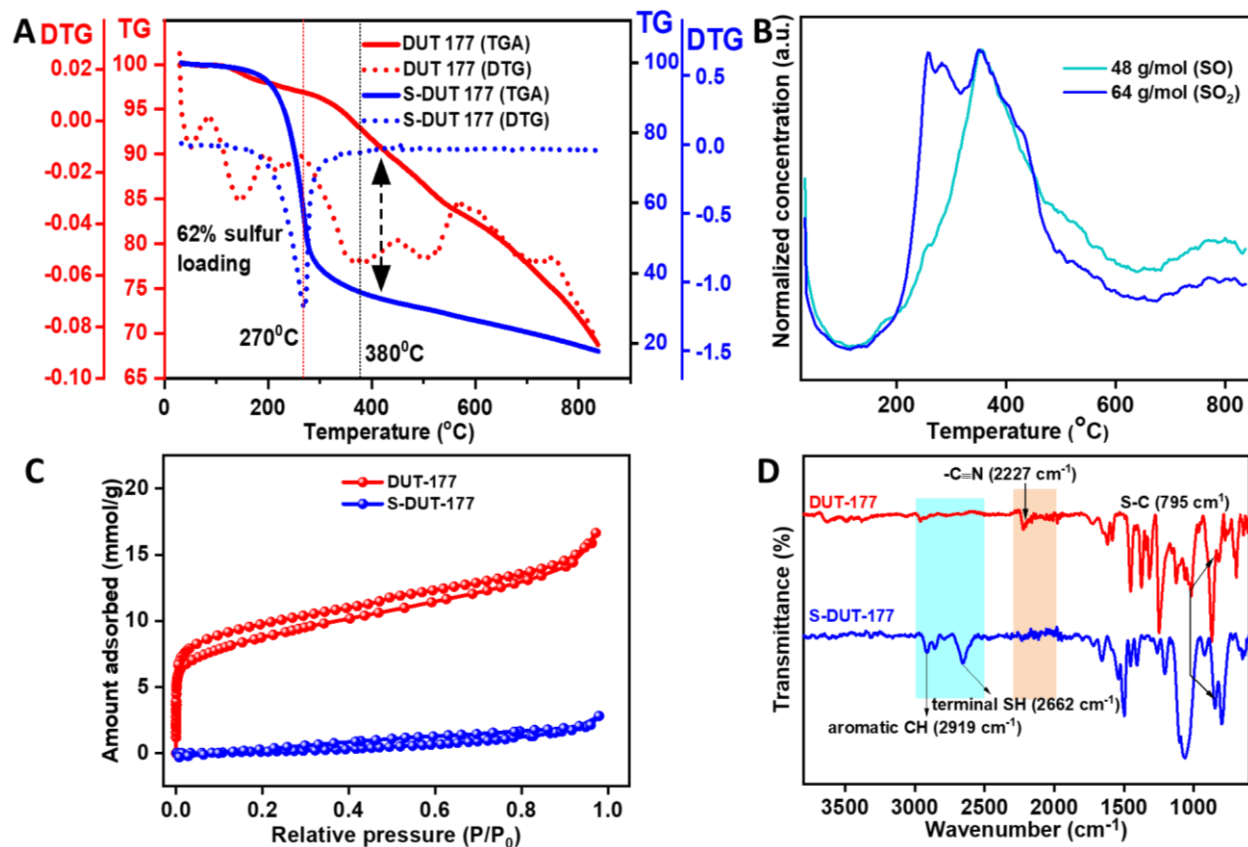


Figure S26. A. TGA-DTA plot of as made DUT-177 and S-DUT-177. B. TGA-MS plot of S-DUT-177 showing two step thermal degradation of the S-DUT-177. C. Physisorption of nitrogen (N<sub>2</sub>) on DUT-177 and S-DUT-177 at 77K. D. IR stretching frequencies of DUT-177 and S-DUT-177 showing the diminishing of the nitrile frequency and appearance of the terminal thiol groups of the polysulfide chains.

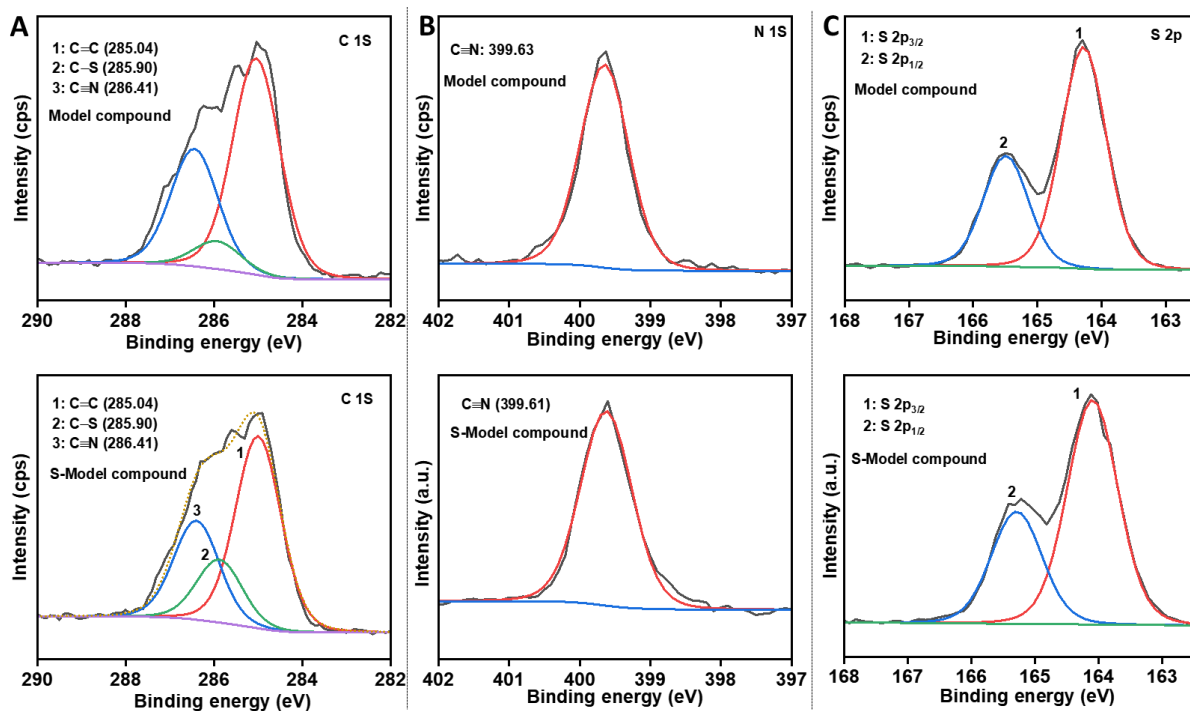


Figure S27. A. X-ray Photoelectron Spectroscopy (XPS) analysis data of (i) C 1s, (ii) N 1s and (iii) S 2p nuclei of model compound before and after sulfurization.

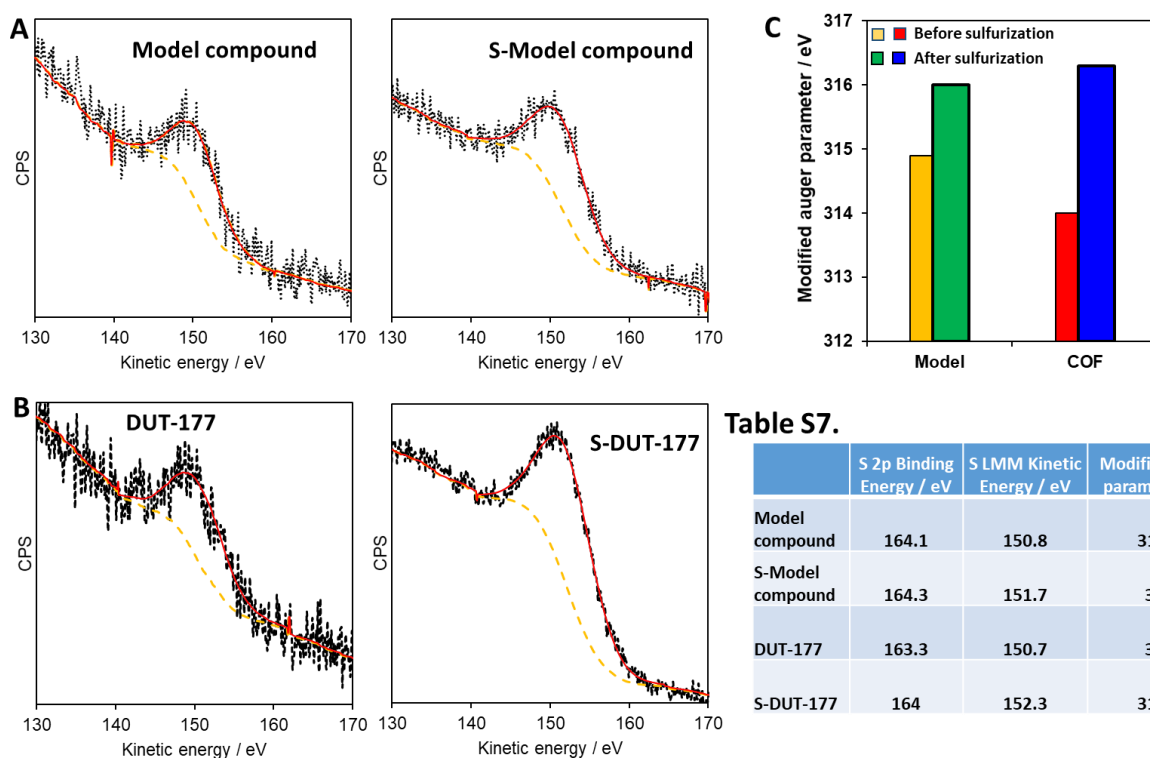


Figure S28. A. Auger Electron Spectroscopy (AES) data of Model compound and S-Model compound. B. AES spectroscopic data of DUT-177 and S-DUT-177. Measurement points are shown in black, fit in red and background in yellow. C. The change of modified Auger parameter ( $a'$ ) before and after sulfurization of model compound and DUT-177.

Table S7. The detailed data obtained from AES experiment.

Table S7.

	S 2p Binding Energy / eV	S LMM Kinetic Energy / eV	Modified Auger parameter / $a'$
Model compound	164.1	150.8	314.9
S-Model compound	164.3	151.7	316
DUT-177	163.3	150.7	314
S-DUT-177	164	152.3	316.3

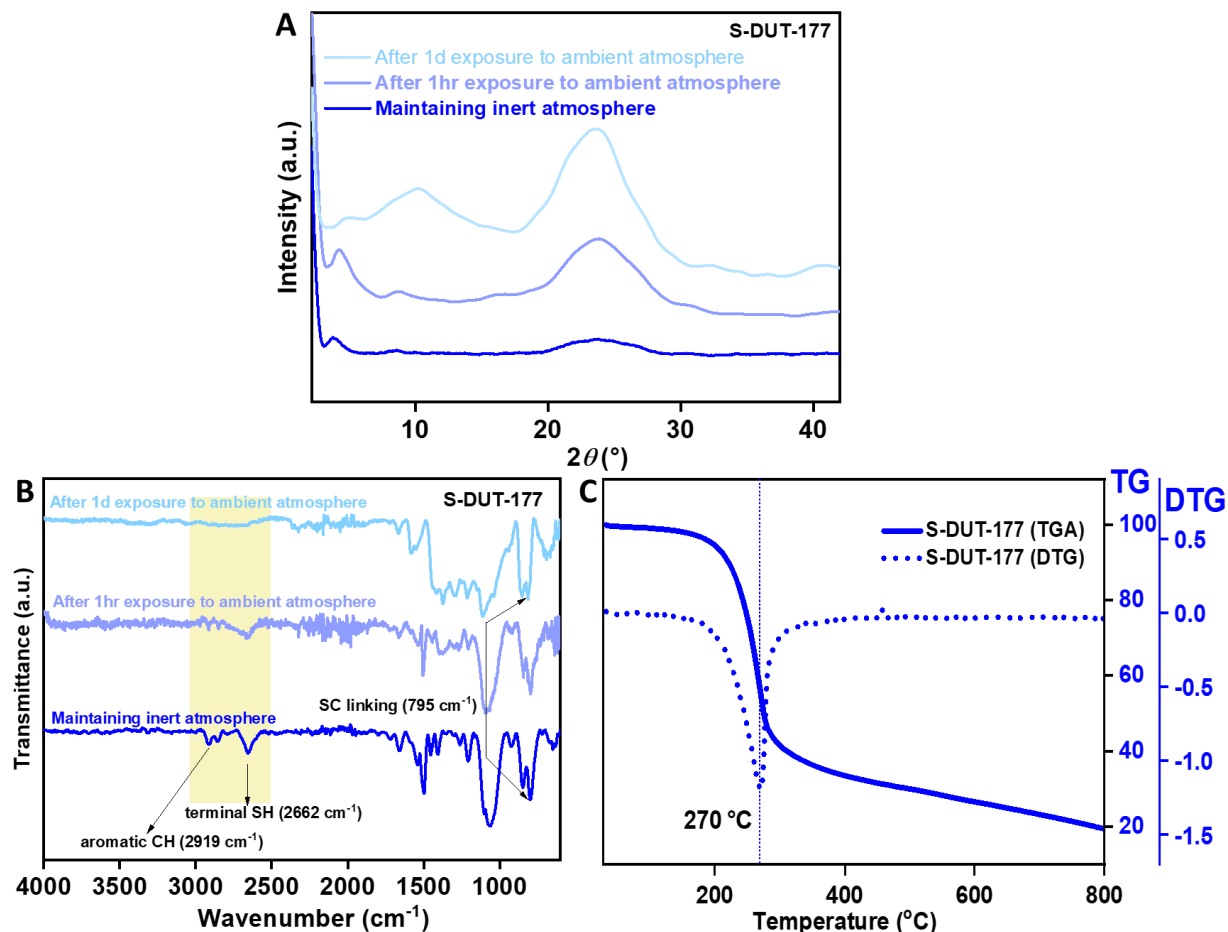


Figure S29. A. PXRD patterns of S-DUT-177 by maintaining inert atmosphere and after exposing to ambient atmosphere. B. The IR stretching bands of S-DUT-177 by maintaining the inert atmosphere and after exposing to ambient atmosphere. C. TGA-DTA plot of as made S-DUT-177.

Table S8. The four probe conductivity measurement data of S-DUT-177

DUT-177	Trial 1	Trial 2	Unit	Formula
Diameter	1	1	cm	d
Area	0,785	0,785	cm <sup>2</sup>	$A=\pi()/4*d^2$
Thickness	0,053	0,07	cm	t
Mass	55	75	mg	m
Density Pellet	1,04	1,07	g / cm <sup>3</sup>	2 ton pressure
Mesurement Range	200	200	MOhm (with 100 nA)	
Resistivity	51,6	65,0	MOhm	R
Resistivity	5,2E+07	6,5E+07	Ohm	R
Spec. Resistivity	7,6E+08	7,3E+08	Ohm*cm	$\rho = R*A/t$
Elec. Conductivity	1,31E-09	1,37E-09	S/cm	$\sigma = 1/\rho$

## XI. Battery performance of DUT-177 and S-DUT-177 derived coin-cell.

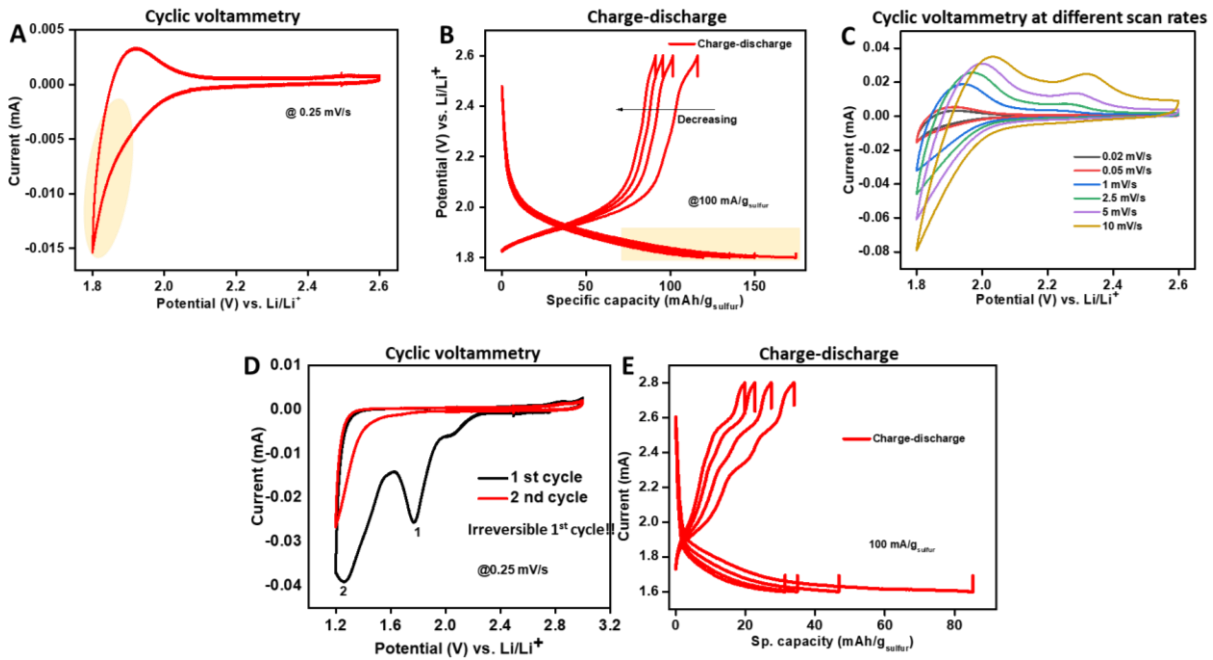


Figure S30. A. CV measurement of DUT-177 derived coin-cell using 1 M LiTFSI in DOL : DME (1:1) with 0.1 M LiNO<sub>3</sub> electrolyte (40  $\mu$ L) at 0.25 mV/s scan rate. B. Charge-discharge plot of DUT-177 derived coin-cell using 1 M LiTFSI in DOL : DME (1:1) with 0.1 M LiNO<sub>3</sub> electrolyte (40  $\mu$ L) at 100 mA/g current density. C. CV measurement plot of DUT-177 derived coin-cell in 1 M LiTFSI in DOL : DME (1:1) with 0.1 M LiNO<sub>3</sub> electrolyte (40  $\mu$ L) at variable scan rate. D. CV measurement plot of DUT-177 derived coin-cell using LiPF<sub>6</sub> in EC : DMC (1:1) electrolyte (40  $\mu$ L) at 0.25 mV/s scan rate. E. Charge-discharge plot of DUT-177 derived coin-cell using LiPF<sub>6</sub> in EC : DMC (1:1) electrolyte (40  $\mu$ L) at 100 mA/g current density.

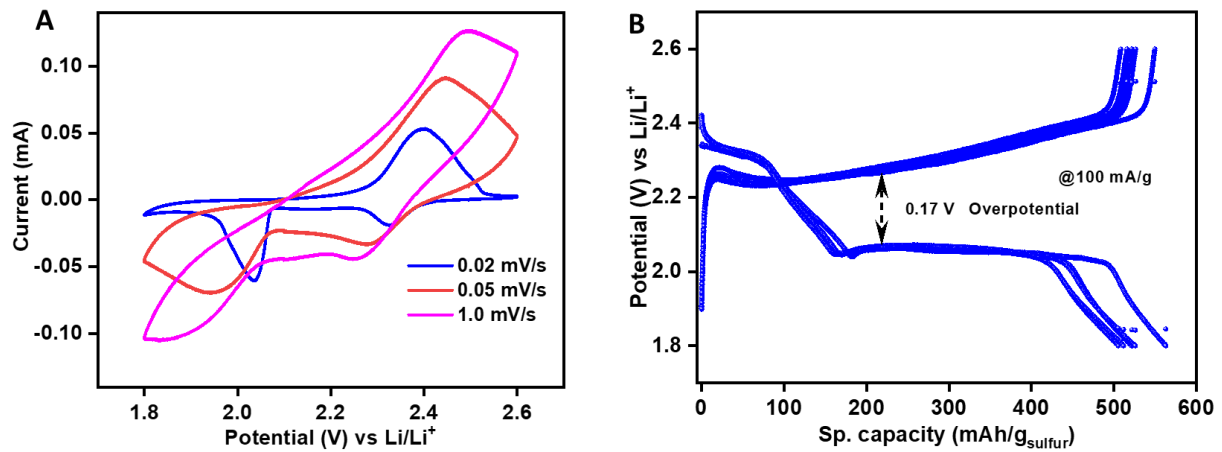


Figure S31: A. Cyclic voltammetry (CV) measurement at different scan rate of S-DUT-177 derived coin-cell in LiTFSI electrolyte. B. Charge-discharge profile of S-DUT-177 derived coin-cell at different current densities in LiTFSI electrolyte.

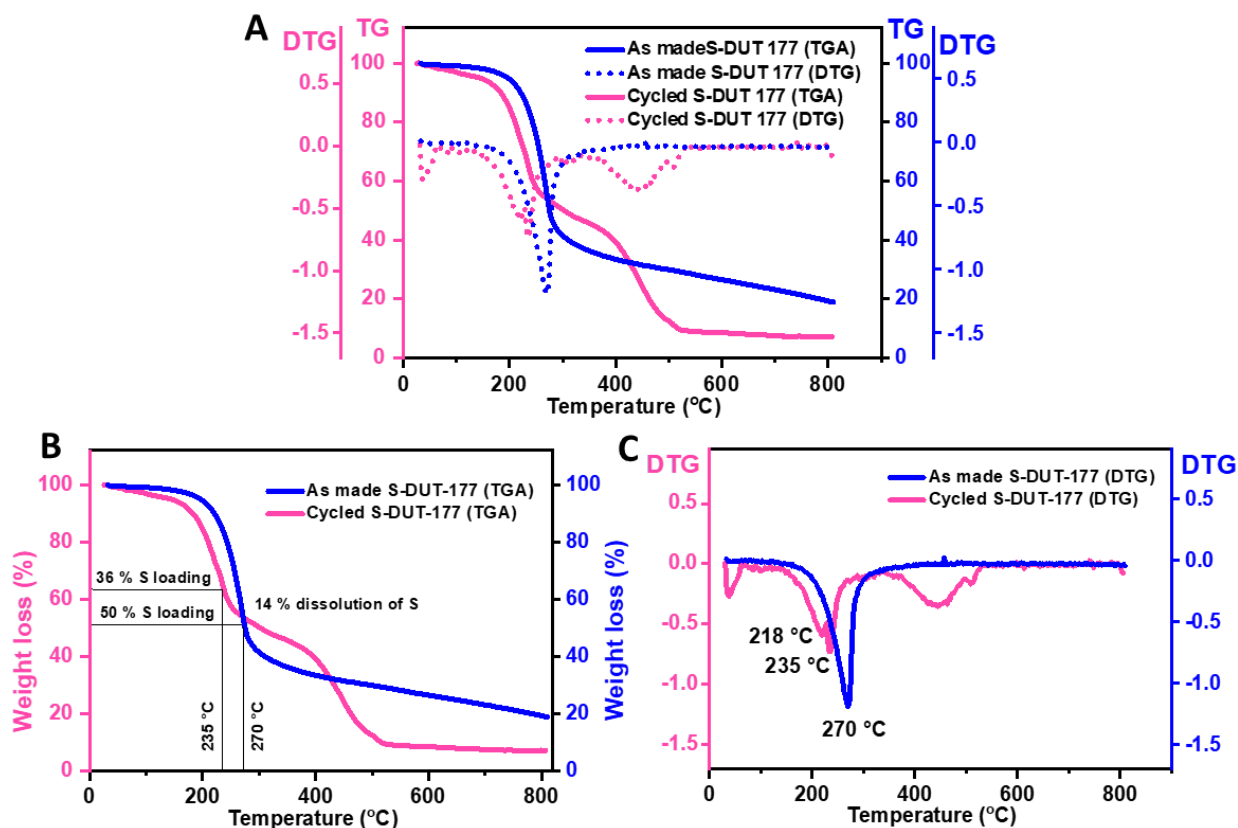


Figure S32. A. Comparison of the TGA-DTA plots of as made S-DUT-177 and battery cycled electrode material derived from S-DUT-177. B. A comparison of the TGA plots of as made S-DUT-177 and battery cycled electrode material derived from S-DUT-177 showing 14 % loss of sulfur loading of S-DUT-177 derived electrode after battery cycling. C. Comparison of the DTA plots of as made S-DUT-177 and battery cycled electrode material derived from S-DUT-177 showing early decomposition of S-DUT-177 derived electrode after battery cycling.

Table S9. Comparison of battery performance of S-DUT-177 with other sulfurized COFs.

COFs	Areal sulfur loading	Sp. capacity @low current density	Sp. capacity @high current density	Retention of capacity	References
S-DUT-177	0.55 mg/cm <sup>2</sup>	720 mAh/g @100 mA/g or at 0.059 C	276 mA/g @1 A/g	76.6 % after 500 cycles at 500 mA/g	This work
COF-F-S	0.50 mg/cm <sup>2</sup>	962 mAh/g @0.1 C	325 mAh/g @2.0 C	64.5 % after 100 cycles at 0.1 C and 51 % after 1000 cycles at 1 C	17
S/CTF-1	0.50 mg/cm <sup>2</sup>	670 mAh/g @0.05 C	406 mAh/g @2.0 C	84.3 % after 50 cycles at 1 C	18
SF-CTF-1s	0.70 mg/cm <sup>2</sup>	850 mAh/g @0.05 C	333 mAh/g @5.0 C	81.6 % after 300 cycles at 1C	19
TPE-TEMPO-POF-F-S	0.70 mg/cm <sup>2</sup>	667 mAh/g @0.1 C	525 mAh/g @1 C	58 % after 350 cycles at 0.1 C	20
COF-ETTA-ETTCA-S	1.3 mg/cm <sup>2</sup>	1617 mAh/g @0.1 C	185 mAh/g @5.0 C	61.5 % after 528 cycles at 0.5 C	21
COF-301@S	1.5 mg/cm <sup>2</sup>	874 mAh/g @0.2 C	691 mAh/g @0.5 C	59.7 % after 500 cycles at 0.5 C	22
PI-COF/S	-----	1205 mAh/g @0.1 C	580 mAh/g @4.0 C	84 % after 500 cycles at 1 C	23
CB-COF	2 mg/cm <sup>2</sup>	1187 mAh/g @0.1 C	562 mAh/g @2.5 C	47 % after 500 cycles at 2.5 C	24
COF-1/S	-----	1411 mAh/g @0.1 C	822 mAh/g @0.5 C	74 % after 500 cycles at 0.5 C	25
Py-COF/S	0.8 mg/cm <sup>2</sup>	1145 mAh/g @0.1 C	659 mAh/g @5.0 C	73.8 % after 550 at 5.0 C	26
GPS	1.15 mg/cm <sup>2</sup>	700 mAh/g @0.1 C	290 mAh/g @2.0 C	52 % after 500 cycles at 0.1 C	27

## Reference

- (1) Sparta, K. M.; Krug, M.; Heinemann, U.; Mueller, U.; Weiss, M. S. XDSAPP2.0. *J. Appl. Cryst.* **2016**, *49*, 1085-1092.
- (2) Sheldrick, G. A short history of SHELX. *Acta Cryst. A* **2008**, *64*, 112-122.
- (3) Kresse, G.; Furthmüller, J. Efficiency of ab-initio total energy calculations for metals and semiconductors using a plane-wave basis set. *Comput. Mater. Sci.* **1996**, *6*, 15-50.
- (4) Kresse, G.; Furthmüller, J. Efficient iterative schemes for ab initio total-energy calculations using a plane-wave basis set. *Phys. Rev. B* **1996**, *54*, 11169-11186.
- (5) Blöchl, P. E. Projector augmented-wave method. *Phys. Rev. B* **1994**, *50*, 17953-17979.
- (6) Kresse, G.; Joubert, D. From ultrasoft pseudopotentials to the projector augmented-wave method. *Phys. Rev. B* **1999**, *59*, 1758-1775.
- (7) Perdew, J. P.; Chevary, J. A.; Vosko, S. H.; Jackson, K. A.; Pederson, M. R.; Singh, D. J.; Fiolhais, C. Atoms, molecules, solids, and surfaces: Applications of the generalized gradient approximation for exchange and correlation. *Phys. Rev. B* **1992**, *46*, 6671-6687.
- (8) Perdew, J. P.; Burke, K.; Ernzerhof, M. Generalized Gradient Approximation Made Simple. *Phys. Rev. Lett.* **1996**, *77*, 3865-3868.
- (9) Grimme, S. Semiempirical GGA-type density functional constructed with a long-range dispersion correction. *J. Comput. Chem.* **2006**, *27*, 1787-1799.
- (10) Heyd, J.; Peralta, J. E.; Scuseria, G. E.; Martin, R. L. Energy band gaps and lattice parameters evaluated with the Heyd-Scuseria-Ernzerhof screened hybrid functional. *J. Chem. Phys.* **2005**, *123*, 174101.
- (11) M. J. Frisch, G. W. T., H. B. Schlegel, G. E. Scuseria, M. A. Robb, J. R. Cheeseman, G. Scalmani, V. Barone, G. A. Petersson, H. Nakatsuji, X. Li, M. Caricato, A. Marenich, J. Bloino, B. G. Janesko, R. Gomperts, B. Mennucci, H. P. Hratchian, J. V. Ortiz, A. F. Izmaylov, J. L. Sonnenberg, D. Williams-Young, F. Ding, F. Lipparini, F. Egidi, J. Goings, B. Peng, A. Petrone, T. Henderson, D. Ranasinghe, V. G. Zakrzewski, J. Gao, N. Rega, G. Zheng, W. Liang, M. Hada, M. Ehara, K. Toyota, R. Fukuda, J. Hasegawa, M. Ishida, T. Nakajima, Y. Honda, O. Kitao, H. Nakai, T. Vreven, K. Throssell, J. A. Montgomery, Jr., J. E. Peralta, F. Ogliaro, M. Bearpark, J. J. Heyd, E. Brothers, K. N. Kudin, V. N. Staroverov, T. Keith, R. Kobayashi, J. Normand, K. Raghavachari, A. Rendell, J. C. Burant, S. S. Iyengar, J. Tomasi, M. Cossi, J. M. Millam, M. Klene, C. Adamo, R. Cammi, J. W. Ochterski, R. L. Martin, K. Morokuma, O. Farkas, J. B. Foresman, and D. J. Fox Gaussian 09, Revision D. 01; Gaussian: Wallingford, CT, 2009.
- (12) Glendening, E. D., Reed, A.E., Carpenter, J.E. and Weinhold, F. NBO Version 3.1. Gaussian Inc., Pittsburgh. **2003**.
- (13) Dong, R.; Han, P.; Arora, H.; Ballabio, M.; Karakus, M.; Zhang, Z.; Shekhar, C.; Adler, P.; Petkov, P. S.; Erbe, A.; Mannsfeld, S. C. B.; Felser, C.; Heine, T.; Bonn, M.; Feng, X.; Cánovas, E. High-mobility band-like charge transport in a semiconducting two-dimensional metal-organic framework. *Nat. Mater.* **2018**, *17*, 1027-1032.
- (14) Dong, R.; Pfeiffermann, M.; Liang, H.; Zheng, Z.; Zhu, X.; Zhang, J.; Feng, X. Large-Area, Free-Standing, Two-Dimensional Supramolecular Polymer Single-Layer Sheets for Highly Efficient Electrocatalytic Hydrogen Evolution. *Angew. Chem., Int. Ed.* **2015**, *54*, 12058-12063.
- (15) Clough, A. J.; Yoo, J. W.; Mecklenburg, M. H.; Marinescu, S. C. Two-Dimensional Metal-Organic Surfaces for Efficient Hydrogen Evolution from Water. *J. Am. Chem. Soc.* **2015**, *137*, 118-121.
- (16) Alla, M.; Lippmaa, E. Resolution limits in magic-angle rotation NMR spectra of polycrystalline solids. *Chem. Phys. Lett.* **1982**, *87*, 30-33.
- (17) Wang, D.-G.; Li, N.; Hu, Y.; Wan, S.; Song, M.; Yu, G.; Jin, Y.; Wei, W.; Han, K.; Kuang, G.-C.; Zhang, W. Highly Fluoro-Substituted Covalent Organic Framework and Its Application in Lithium-Sulfur Batteries. *ACS Appl. Mater. Interfaces* **2018**, *10*, 42233-42240.
- (18) Talapaneni, S. N.; Hwang, T.H.; Je, S. H.; Buyukcakir, O.; Choi, J. W.; Coskun, A. Elemental-Sulfur-Mediated Facile Synthesis of a Covalent Triazine Framework for High-Performance Lithium-Sulfur Batteries. *Angew. Chem., Int. Ed.* **2016**, *55*, 3106.
- (19) Je, H. S. H.; Kim, H. J.; Kim, J.; Choi, J. W.; Coskun, A. Perfluoroaryl-Elemental Sulfur  $S_NAr$  Chemistry in Covalent Triazine Frameworks with High Sulfur Contents for Lithium-Sulfur Batteries. *Adv. Funct. Mater.* **2017**, *27*, 1703947.
- (20) Zhou, B.; Hu, X.; Zeng, G.; Li, S.; Wen, Z.; Chen, L. Bottom-Up Construction of Porous Organic Frameworks with Built-In TEMPO as a Cathode for Lithium-Sulfur Batteries. *ChemSusChem* **2017**, *10*, 2955.
- (21) Lu, B.-Y.; Wang, Z.-Q.; Cui, F.-Z.; Li, J.-Y.; Han, X.-H.; Qi, Q.-Y.; Ma, D.-L.; Jiang, G.-F.; Zeng, X.-X.; Zhao, X. A Covalent Organic Framework with Extended  $\pi$ -Conjugated Building Units as a Highly Efficient Recipient for Lithium-Sulfur Batteries. *ACS Appl. Mater. Interfaces* **2020**, *12*, 34990-34998.
- (22) Li, Z.; Zhou, H.-Y.; Zhao, F.-L.; Wang, T.-X.; Ding, X.; Han, B.-H.; Feng, W. Three-dimensional Covalent Organic Frameworks as Host Materials for Lithium-Sulfur Batteries. *Chin. J. Polym. Sci.* **2020**, *38*, 550-557.
- (23) Duan, H.; Li, K.; Xie, M.; Chen, J.-M.; Zhou, H.-G.; Wu, X.; Ning, G.-H.; Cooper, A. I.; Li, D. Scalable Synthesis of Ultrathin Polyimide Covalent Organic Framework Nanosheets for High-Performance Lithium-Sulfur Batteries. *J. Am. Chem. Soc.* **2021**, *143*, 19446-19453.

- (24) Zhu, Y.; Yang, J.; Qiu, X.; Li, M.; He, G.; Wang, Q.; Xie, Z.; Li, X.; Yu, H. Amphiphilic Carborane-Based Covalent Organic Frameworks as Efficient Polysulfide Nano-Trappers for Lithium–Sulfur Batteries. *ACS Appl. Mater. Interfaces* **2021**, *13*, 60373-60383.
- (25) Ghazi, Z. A.; Zhu, L.; Wang, H.; Naeem, A.; Khattak, A. M.; Liang, B.; Khan, N. A.; Wei, Z.; Li, L.; Tang, Z. Efficient Polysulfide Chemisorption in Covalent Organic Frameworks for High-Performance Lithium-Sulfur Batteries. *Adv. Energy Mat.* **2016**, *6*, 1601250.
- (26) Meng, Y.; Lin, G.; Ding, H.; Liao, H.; Wang, C. Impregnation of sulfur into a 2D pyrene-based covalent organic framework for high-rate lithium–sulfur batteries. *J. Mater. Chem. A* **2018**, *6*, 17186-17191.
- (27) Tantis, I.; Bakandritsos, A.; Zaoralová, D.; Medved', M.; Jakubec, P.; Havláková, J.; Zbořil, R.; Otyepka, M. Covalently Interlinked Graphene Sheets with Sulfur-Chains Enable Superior Lithium–Sulfur Battery Cathodes at Full-Mass Level. *Adv. Funct. Mater.* **2021**, *31*, 2101326.